

1 **Relating geostationary satellite measurements of aerosol optical**
2 **depth (AOD) over East Asia to fine particulate matter (PM_{2.5}):**
3 **insights from the KORUS-AQ aircraft campaign and GEOS-**
4 **Chem model simulations**

5 Shixian Zhai¹, Daniel J. Jacob¹, Jared F. Brewer¹, Ke Li¹, Jonathan M. Moch¹, Jhoon Kim^{2,3},
6 Seoyoung Lee², Hyunkwang Lim², Hyun Chul Lee³, Su Keun Kuk³, Rokjin J. Park⁴, Jaemin I.
7 Jeong⁴, Xuan Wang⁵, Pengfei Liu⁶, Gan Luo⁷, Fangqun Yu⁷, Jun Meng⁸, Randall V. Martin⁹,
8 Katherine R. Travis¹⁰, Johnathan W. Hair¹⁰, Bruce E. Anderson¹⁰, Jack E. Dibb¹¹, Jose L.
9 Jimenez¹², Pedro Campuzano-Jost¹², Benjamin A. Nault^{12, a}, Jung-Hun Woo¹³, Younha Kim¹⁴,
10 Qiang Zhang¹⁵, Hong Liao¹⁶

11 ¹Harvard John A. Paulson School of Engineering and Applied Sciences, Harvard University, Cambridge, MA, USA

12 ²Department of Atmospheric Sciences, Yonsei University, Seoul, Republic of Korea

13 ³Samsung Particulate Matter Research Institute, Samsung Advanced Institute of Technology, 130 Samsung-ro,
14 Yeongtong-gu, Suwon-si, Gyeonggi-do, Republic of Korea

15 ⁴School of Earth and Environmental Sciences, Seoul National University, Seoul, Republic of Korea

16 ⁵School of Energy and Environment, City University of Hong Kong, Hong Kong SAR, China

17 ⁶School of Earth and Atmospheric Sciences, Georgia Institute of Technology, Atlanta, GA, USA

18 ⁷Atmospheric Sciences Research Center, University at Albany, Albany, New York, USA

19 ⁸Department of Atmospheric & Oceanic Sciences, University of California, Los Angeles, California, USA

20 ⁹Department of Energy, Environmental & Chemical Engineering, Washington University in St Louis, MO, USA

21 ¹⁰NASA Langley Research Center, Hampton, VA, USA

22 ¹¹Institute for the Study of Earth, Oceans, and Space, University of New Hampshire, Durham, NH, USA

23 ¹²Department of Chemistry, and Cooperative Institute for Research in Environmental Sciences, University of
24 Colorado, Boulder, CO, USA

25 ¹³Department of Civil and Environmental Engineering, Konkuk University, Seoul, Republic of Korea

26 ¹⁴International Institute for Applied Systems Analysis (IIASA), 2361 Laxenburg, Austria

27 ¹⁵Department of Earth System Science, Tsinghua University, Beijing, China.

28 ¹⁶Jiangsu Key Laboratory of Atmospheric Environment Monitoring and Pollution Control, Collaborative Innovation
29 Center of Atmospheric Environment and Equipment Technology, School of Environmental Science and
30 Engineering, Nanjing University of Information Science and Technology, Nanjing, China.

31 ^a Now at Center for Aerosol and Cloud Chemistry, Aerodyne Research, Inc., Billerica, MA, USA

32 *Correspondence:* Shixian Zhai (zhaisx@g.harvard.edu)

33

34 **Abstract.** Geostationary satellite measurements of aerosol optical depth (AOD) over East Asia from the GOCI and
35 AHI instruments can augment surface monitoring of fine particulate matter (PM_{2.5}) air quality, but this requires
36 better understanding of the AOD-PM_{2.5} relationship. Here we use the GEOS-Chem chemical transport model to
37 analyze the critical variables determining the AOD-PM_{2.5} relationship over East Asia by simulation of observations
38 from satellite, aircraft, and ground-based datasets. This includes the detailed vertical aerosol profiling over South
39 Korea from the KORUS-AQ aircraft campaign (May-June 2016) with concurrent ground-based PM_{2.5} composition,
40 PM₁₀, and AERONET AOD measurements. The KORUS-AQ data show that 550 nm AOD is mainly contributed by
41 sulfate-nitrate-ammonium (SNA) and organic aerosols in the planetary boundary layer (PBL), despite large dust
42 concentrations in the free troposphere, reflecting the optically effective size and high hygroscopicity of the PBL
43 aerosols. We updated SNA and organic aerosol size distributions in GEOS-Chem to represent aerosol optical
44 properties over East Asia by using in-situ measurements of particle size distributions from KORUS-AQ. We find
45 that SNA and organic aerosols over East Asia have larger size (number median radius of 0.11 μm with geometric
46 standard deviation of 1.4) and 20% larger mass extinction efficiency as compared to aerosols over North America
47 (default setting in GEOS-Chem). Although GEOS-Chem is successful in reproducing the KORUS-AQ vertical
48 profiles of aerosol mass, its ability to link AOD to PM_{2.5} is limited by under-accounting of coarse PM and by a large
49 overestimate of nighttime PM_{2.5} nitrate. The GOCI/AHI AOD data over East Asia in different seasons show
50 agreement with AERONET AODs and a spatial distribution consistent with surface PM_{2.5} network data. The AOD
51 observations over North China show a summer maximum and winter minimum, opposite in phase to surface PM_{2.5}.
52 This is due to low PBL depths compounded by high residential coal emissions in winter, and high relative humidity
53 (RH) in summer. Seasonality of AOD and PM_{2.5} over South Korea is much weaker, reflecting weaker variation of
54 PBL depth and lack of residential coal emissions.

55 **1 Introduction**

56 PM_{2.5} (particulate matter with aerodynamic diameter less than 2.5 μm) in surface air is a severe public health
57 concern in East Asia, but surface monitoring networks are too sparse to thoroughly assess population exposure.
58 Satellite observations of aerosol optical depth (AOD) can provide a valuable complement (Van Donkelaar et al.,
59 2015). Geostationary satellite sensors, including the Geostationary Ocean Color Imager (GOCI) launched by the
60 Korea Aerospace Research Institute (KARI) in 2011 (Choi et al., 2016, 2018, 2019) and the Advanced Himawari
61 Imager (AHI) launched by the Japanese Meteorological Agency (JMA) in 2014 (Lim et al., 2018, 2021), offer the
62 potential for high-density mapping of PM_{2.5} over East Asia (Chen et al., 2019; Wei et al., 2021a). However, more
63 confidence is needed in relating AOD to PM_{2.5}. Here we evaluate the capability of the GEOS-Chem chemical
64 transport model (CTM) to simulate AOD-PM_{2.5} relationships over East Asia, exploiting in-situ aircraft
65 measurements of vertical aerosol profiles and optical properties from the joint NASA-NIER Korea - United States
66 Air Quality (KORUS-AQ) field study in May-June 2016 (Crawford et al., 2021; Peterson et al., 2019; Jordan et al.,
67 2020) together with GOCI/AHI geostationary satellite data and surface measurement networks. This enables us to
68 identify critical variables and uncertainties for inferring PM_{2.5} from satellite AOD data.

69 A number of past studies have used satellite AOD data to infer surface $PM_{2.5}$ using physical and statistical models.
70 The standard geophysical approach has been to use a CTM, such as GEOS-Chem, to compute the $PM_{2.5}/AOD$ ratio
71 (Liu et al., 2004; van Donkelaar et al., 2006; van Donkelaar et al., 2015; Xu et al., 2015; Geng et al., 2017), with
72 recent applications correcting for CTM biases using available $PM_{2.5}$ surface network data (Brauer et al., 2016; Van
73 Donkelaar et al., 2016; van Donkelaar et al., 2019; Hammer et al., 2020). An alternative approach is to use artificial
74 intelligence algorithms to relate satellite AOD to $PM_{2.5}$ by training on the surface network data (Hu et al., 2017;
75 Chen et al., 2018; Xiao et al., 2018; Wei et al., 2021a; Wei et al., 2021b; Pendergrass et al., 2021), and sometimes
76 including CTM values as predictors (Di et al., 2019; Xue et al., 2019). Yet another approach is to assimilate the
77 satellite-measured AODs in a CTM and correct in this manner the $PM_{2.5}$ simulation, although this requires
78 attribution of model AOD errors to specific model parameters (Kumar et al., 2019; Saide et al., 2014; Sekiyama et
79 al., 2010; Cheng et al., 2019). In all of these approaches, a better physical understanding of the AOD- $PM_{2.5}$
80 relationship as simulated by CTMs can greatly enhance the capability to infer $PM_{2.5}$ from AOD data.

81 AOD measures aerosol extinction (scattering and absorption) integrated over the atmospheric column, so that its
82 relationship to 24-hr average surface $PM_{2.5}$ (the standard air quality metric) depends on the aerosol vertical
83 distribution and optical properties, ambient relative humidity (RH), diurnal variation of $PM_{2.5}$, and contribution from
84 coarse particulate matter to AOD. Airborne measurements of aerosol vertical profiles (without species information)
85 in East Asia are limited (Zhang et al., 2006; Liu et al., 2009; Zhang et al., 2009; Sun et al., 2013; Li et al., 2017), and
86 speciated vertical profiles are rarer. AOD is highly sensitive to RH (Brock et al., 2016; Latimer and Martin et al.,
87 2019; Saide et al., 2020), but the impact from RH uncertainty on AOD simulation lacks evaluation. In addition,
88 because the AOD is a daytime measurement that needs to be related to 24-h average $PM_{2.5}$, the diurnal variation of
89 $PM_{2.5}$ needs to be understood (Guo et al., 2017; Lennartson et al., 2018). Finally, although there are studies on the
90 optical depth of coarse mode desert dust (Eck et al., 2010; Ridley et al., 2016), there has been to our knowledge no
91 study of how coarse anthropogenic PM may contribute to the AOD measurements. Coarse anthropogenic PM
92 (distinct from desert dust) is known to be high over East Asia (Chen et al., 2015; Dai et al., 2018).

93 **2 Data and methods**

94 **2.1 Observations**

95 We use observations over China and South Korea from multiple platforms including surface sites, aircraft, and
96 satellites (Table 1 and 2). Surface data (Table 1) include $PM_{2.5}$ from national observation networks in China (Zhai et
97 al., 2019) and South Korea (Jordan et al., 2020), speciated $PM_{2.5}$ at 7 supersites in South Korea during KORUS-AQ
98 (Choi et al., 2019), and ground-based AODs from the AERONET network at 5 sites in East China and 10 sites in
99 South Korea (21 sites during KORUS-AQ). We use total and fine-mode AODs at 500 nm wavelength from the
100 AERONET Version 3; Spectral Deconvolution Algorithm (SDA) Version 4.1 Retrieval Level 2.0 database (Giles et
101 al., 2019; O'Neill et al., 2003). The AERONET AODs at 500 nm are converted to 550 nm using total and fine mode
102 Ångström Exponents at 500 nm for consistency with the satellite AOD data.

103 **Table 1. Surface site observations used in this work (2016)**

Variable	Number of sites
PM _{2.5} in East China ^a	598
PM _{2.5} in South Korea ^b	130
PM _{2.5} composition in South Korea (May-June 2016) ^c	7
AERONET total and fine mode AOD in East China ^d	5
AERONET total and fine mode AOD in South Korea ^d	10-21 ^e

104 ^a Hourly PM_{2.5} from the China National Environmental Monitoring Centre (CNEMC; quotsoft.net/air/) in East
 105 China, including only sites with more than 90% data coverage in each month of 2016. Quality control of the
 106 CNEMC dataset is described in our previous study (Zhai et al., 2019). The PM_{2.5} measurements are made at
 107 reference RH ≤ 35%.

108 ^b Hourly PM_{2.5} from the AirKorea network (airkorea.or.kr), with the same data selection criteria as for East China.
 109 The PM_{2.5} measurements are made at reference RH ≤ 35%.

110 ^c Major PM_{2.5} components including sulfate, nitrate, ammonium, organic carbon, and black carbon at 7 supersites in
 111 South Korea during KORUS-AQ (May-June 2016; Choi et al., 2019). The mass concentration of organic carbon is
 112 converted to that of organic aerosol with a multiplicative factor of 1.8 based on KORUS-AQ observations (Kim et
 113 al., 2018).

114 ^d AODs are from the AERONET Version 3 Level 2.0 all-points database (aeronet.gsfc.nasa.gov), except that AODs
 115 at the XuZhou site in East China are from the Version 3 Level 1.5 database. AOD at 500 nm (AOD_{500nm}) is
 116 converted to 550 nm (AOD_{550nm}) using Ångström Exponent at 500 nm (AE_{500nm}) following: $AOD_{550nm} =$
 117 $AOD_{500nm} \left(\frac{550}{500}\right)^{-AE_{500nm}}$.

118 ^e AERONET AODs in South Korea are from 10 sites for the full year of 2016 and 21 sites during KORUS-AQ.

119 The KORUS-AQ campaign (Table 2) includes 20 flights over the Korean peninsula and the surrounding ocean from
 120 May 2 to June 10, 2016, with vertical profiling up to 8 km altitude. We use the aircraft observations of remote and in
 121 situ aerosol extinction (scattering + absorption) coefficients, dry aerosol number size distributions, sub-micron non-
 122 refractory aerosol composition, bulk aerosol ionic composition, black carbon (BC), and relative humidity (RH).

123 Geostationary satellite AOD at 550 nm are retrieved by the Yonsei Aerosol Retrieval (YAER) algorithm for the
 124 GOCI (Choi et al., 2016, 2018) and AHI (Lim et al. 2018) instruments, with GOCI covering East China and South
 125 Korea and AHI covering the broad East Asia region. AOD from GOCI and AHI have a 6 km × 6 km spatial
 126 resolution and 2.5-minute (AHI) to 1-hour (GOCI) temporal resolution for 8 hours per day (09:30 to 16:30 local
 127 time). We use the fused AOD product generated from the Yonsei GOCI and AHI AOD retrievals, each using two
 128 different surface reflectance methods (Lim et al., 2021). Fusion of this four-member ensemble is done by the
 129 maximum likelihood estimate (MLE) method, with weighting and averaging based on errors determined by
 130 comparison to AERONET AOD. The fused satellite AOD product is shown by Lim et al. (2021) to have higher
 131 accuracy than its member products in comparison with AERONET data during the KORUS-AQ campaign. We will
 132 refer to it as the ‘GEO satellite AOD’ product in what follows.

133 **Table 2. KORUS-AQ aircraft observations used in this work (May-June 2016).**

Variable	Instrument
Aerosol extinction profile at 532 nm	HSRL ^a
Aerosol scattering coefficient at 550 nm	TSI nephelometers ^b
Aerosol absorption coefficient at 532 nm	PSAPs ^c
Aerosol dry size distribution	TSI LAS ^d
Bulk aerosol ionic composition	SAGA ^e
Sub-micron non-refractory aerosol composition	HR-ToF-AMS ^f
Black carbon concentration	HDSP2 ^g
Relative humidity	DLH ^h

134 ^a NASA Langley airborne High Spectral Resolution Lidar (HSRL) (Hair et al., 2008; Scarino et al., 2014).

135 ^b NASA Langley TSI-3563 nephelometers (Ziemba et al., 2013).

136 ^c Radiance Research 3-wavelength particle soot absorption photometers (PSAPs; Ziemba et al., 2013).

137 ^d In-situ particle size distributions over the 0.1-5.0 μm diameter range from the TSI Laser Aerosol Spectrometer
138 (LAS) Model 3340.

139 ^e University of New Hampshire (UNH) Soluble Acidic Gases and Aerosol (SAGA) instrument (Dibb et al., 2003).
140 The cutoff aerodynamic diameter of the inlet is around 4 μm , corresponding to a geometric particle diameter of 2.5
141 μm (McNaughton et al., 2007; McNaughton et al., 2009).

142 ^f University of Colorado Boulder High-Resolution Time-of-Flight Aerosol Mass Spectrometer (HR-ToF-AMS;
143 DeCarlo et al., 2006; Nault et al., 2018; Guo et al., 2020).

144 ^g NOAA Humidified-Dual-Single-Particle Soot Photometer (HDSP2; Lamb et al., 2018).

145 ^h NASA Diode Laser Hygrometer (DLH; Podolske et al., 2003).

146 **2.2 GEOS-Chem simulation**

147 We use GEOS-Chem version 12.7.1 (DOI: 10.5281/zenodo.3676008) in a nested-grid simulation at a horizontal
148 resolution of $0.5^\circ \times 0.625^\circ$ over East Asia (100-145 $^\circ\text{E}$, 20-50 $^\circ\text{N}$). GEOS-Chem simulates detailed tropospheric
149 oxidant-aerosol chemistry and is driven here by GEOS-FP assimilated meteorological data from the NASA Global
150 Modeling and Assimilation Office (GMAO). Boundary layer mixing uses the non-local scheme implemented by Lin
151 and McElroy (2010). Dry deposition of gases and particles follows a standard resistance-in-series scheme (Zhang et
152 al., 2001; Fairlie et al., 2007; Fisher et al., 2011; Jaeglé et al., 2018). Wet deposition of gases and particles includes
153 contributions from rainout, washout, and scavenging in convective updrafts (Liu et al., 2001; Amos et al., 2012; Q.
154 Wang et al., 2011; Q. Wang et al., 2014) with recent updates by Luo et al. (2019, 2020). We use pre-archived initial

155 conditions from Zhai et al. (2021) and run the model from December 1, 2015 to December 31, 2016. The first month
156 is used for spin-up and the year 2016 is used for analysis.

157 GEOS-Chem has been used extensively to simulate PM_{2.5} and its composition in East Asia (Geng et al., 2017; Li et
158 al., 2016; Choi et al., 2019; Jeong et al., 2008; Park et al., 2021; Zhai et al., 2021). Here we use the bulk
159 representation of aerosols including sulfate (Park et al., 2004; Alexander et al., 2009), nitrate (Jaeglé et al., 2018),
160 primary and secondary organics (Pai et al., 2020), BC (Q. Wang et al., 2014), natural dust in four advected size
161 ranges (Fairlie et al., 2007), anthropogenic fine dust (Philip et al., 2017), and sea salt in two size ranges (Jaeglé et
162 al., 2011). Heterogeneous sulfate formation on aqueous aerosols is represented by a simplified parameterization
163 scheme (Y. Wang et al., 2014), where the SO₂ uptake coefficient (γ) linearly increases from 1×10^{-5} at RH \leq 50% to
164 2×10^{-5} at RH = 100%. The thermodynamic equilibrium of sulfate-nitrate-ammonium (SNA) aerosols with the gas
165 phase is computed with ISORROPIA II (Fountoukis and Nenes, 2007; Pye et al., 2009) assuming an aqueous
166 aerosol. We include reactive uptake on dust of acid gases (HNO₃, SO₂, and H₂SO₄), limited by consumption of dust
167 alkalinity (Fairlie et al., 2010). The alkalinity of emitted dust is estimated by assuming 7.1% Ca²⁺ and 1.1% Mg²⁺ as
168 alkaline cations by dust mass (Shah et al., 2020).

169 Monthly anthropogenic emissions are from the Multi-resolution Emission Inventory in 2016 for China (MEIC;
170 Zheng et al., 2018; <http://meicmodel.org>) and from the KORUSv5 emission inventory at base year 2015 (Woo et al.,
171 2020; http://aisl.konkuk.ac.kr/#/emission_data/korus-aq_emissions) for other Asian countries and shipping
172 emissions. MEIC over China applies weekly and diurnal scaling factors for all anthropogenic emissions (Zheng et
173 al., 2018). The KORUSv5 agricultural NH₃ emissions apply the diurnal scaling factors from MEIC. Natural
174 emissions include NO_x from lightning (Murray et al., 2012) and soil (Hudman et al., 2012), MEGANv2 biogenic
175 volatile organic compounds (VOCs) (Guenther et al., 2012), dust (Meng et al., 2020), and sea salt (Jaeglé et al.,
176 2011). Open fire emissions are from the Global Fire Emissions Database version 4 (GFED4; van der Werf et al.,
177 2017).

178 **2.3 AOD simulation**

179 AOD in GEOS-Chem is diagnosed by integrating vertically the aerosol scattering and absorption coefficients
180 obtained with a standard Mie calculation applied to assumed size distributions, hygroscopicity, refractive indices,
181 and densities for individual aerosol components, and summing over all components (Martin et al., 2003). Optical
182 properties are listed in Table 3. Sulfate, nitrate, and ammonium share the same optical properties and are lumped as
183 an SNA aerosol component for the purpose of optical calculations. All aerosol components except dust are assumed
184 to follow log-normal size distributions. Dust includes 7 size bins (centered at radii of 0.15, 0.25, 0.4, 0.8, 1.5, 2.5,
185 and 4.0 μm) for optical calculations, with the smallest four bins partitioned by mass from the first advected dust bin
186 ($< 2.5 \mu\text{m}$ in geometric diameter) following L. Zhang et al. (2013). Dust particles follow a gamma size distribution
187 within their optical size bins (Curci, 2012). The BC absorption enhancement from coating is as given by X. Wang et
188 al. (2014).

189 Our initial simulations indicated that aerosol extinction coefficients from the standard GEOS-Chem version 12.7.1
 190 underestimated in situ measured extinction coefficients during KORUS-AQ by 20% on average (Figure S1). We
 191 traced this problem to bias in the assumed size distributions for SNA and organic aerosol, as shown in Section 3.
 192 Therefore, we re-computed the diagnostic AOD using updated log-normal size distributions for SNA and organic
 193 aerosol with number median radius $R_{N,med} = 0.11 \mu\text{m}$ and geometric standard deviation $\sigma = 1.4$ based on KORUS-
 194 AQ observations, instead of $R_{N,med} = 0.058 \mu\text{m}$ and $\sigma = 1.6$ in the standard model version 12.7.1, which is derived
 195 from IMPROVE network measurements of aerosol mass scattering efficiency over North America (Latimer and
 196 Martin, 2019).

197 **Table 3. Aerosol optical properties ^a.**

Aerosol component	$R_{N,med}$, μm	σ	Hygroscopicity ^b	Refractive index	ρ , g cm^{-3}
SNA ^c	0.11	1.4	$\kappa = 0.61$	$1.53 - 6.0 \times 10^{-3}i$	1.7
Organic ^c	0.11	1.4	$\kappa = 0.1$	$1.53 - 6.0 \times 10^{-3}i$	1.3
BC	0.020	1.6	GADS	$1.75 - 4.4 \times 10^{-3}i$	1.8
Sea salt (fine)	0.085	1.5	GADS	$1.5 - 1.0 \times 10^{-3}i$	2.2
Sea salt (coarse)	0.40	1.8	GADS	$1.5 - 1.0 \times 10^{-3}i$	2.2
Dust	7 size bins	NA	$\kappa = 0$ ^d	$1.558 - 1.4 \times 10^{-3}i$	2.5-2.65 ^e

198 ^a Aerosol optical properties used in this work for computing aerosol scattering and absorption coefficients. Values
 199 are from the standard GEOS-Chem model version 12.7.1, except for the size distributions of SNA and organic
 200 aerosol which are based on KORUS-AQ observations (see text). All aerosol components except dust have log-
 201 normal dry size distributions where $R_{N,med}$ is the number median radius and σ is the geometric standard deviation.
 202 Refractive indices are for 550 nm wavelength. ρ is the dry aerosol mass density.

203 ^b Hygroscopic growth for SNA and organic aerosol as a function of relative humidity (RH, %) is computed from κ -
 204 Kohler theory as a diameter growth factor $GF = (1 + \kappa * RH/(100-RH))^{1/3}$ (Latimer and Martin, 2019). Hygroscopic
 205 growth factors for other aerosol components are from the Global Aerosol Data Set (GADS) as tabulated in Chin et
 206 al. (2002) and Martin et al. (2003).

207 ^c $R_{N,med}$ and σ are fit to KORUS-AQ observations as described in the text. Standard GEOS-Chem v12.7.1 assumes
 208 $R_{N,med} = 0.058 \mu\text{m}$, $\sigma = 1.6$ (Latimer and Martin, 2019).

209 ^d Hygroscopic growth of dust particles is assumed negligible.

210 ^e Sub-micron dust particles have a density of 2.5 g cm^{-3} while coarse mode dust particles have a density of 2.65 g
 211 cm^{-3} . Dust size distribution is described in the text.

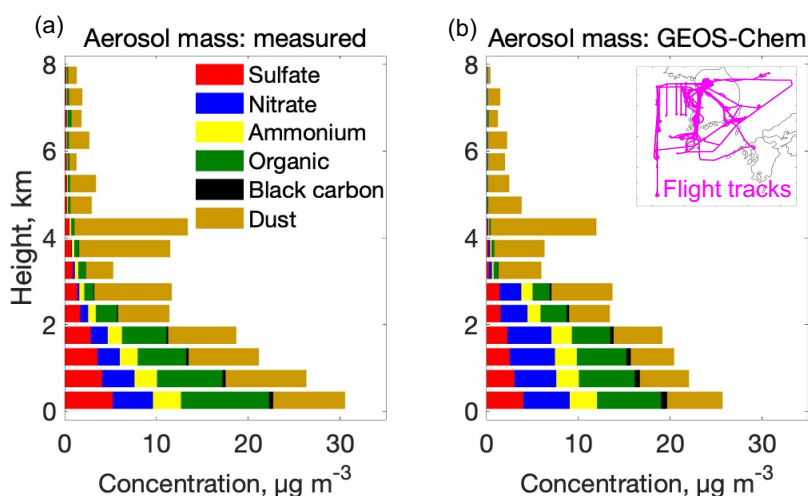
212 3 Aerosol concentrations and optical properties during KORUS-AQ

213 Here we use the KORUS-AQ aircraft observations and their simulation with GEOS-Chem to better understand the
 214 vertical distributions of different aerosol components contributing to AOD over South Korea. We begin with the
 215 mean vertical profile of aerosol mass and go on to examine the aerosol optical properties. This provides the basis for
 216 analyzing the observed vertical profile of aerosol extinction, its simulation by GEOS-Chem, and the consistency
 217 with GEO satellite and AERONET AOD measurements over South Korea during the KORUS-AQ period.

218 3.1 Vertical profile of aerosol mass

219 Figure 1 shows the mean aircraft vertical profiles of aerosol mass observed during KORUS-AQ and their simulation
 220 by GEOS-Chem. The KORUS-AQ aircraft sampled during the daytime, mainly between 9 am and 3 pm local time.
 221 Here and elsewhere, the model is sampled along the flight tracks and at the flight times. The observed vertical
 222 distribution of aerosol mass concentrations (Figure 1a) shows that 58% of column aerosol mass is below 2 km
 223 altitude, which we define as the average planetary boundary layer (PBL) during KORUS-AQ, and 34% is at 2-5 km
 224 altitude, which we define as the lower free troposphere (FT). The model has a similar vertical distribution (Figure
 225 1b), with 57% of aerosol mass in the PBL and 36% in the lower FT. SNA, organic, and dust each contribute about a
 226 third of aerosol mass in the PBL while dust dominates in the lower FT both in the observations and in the model.
 227 The enhanced dust in the lower FT is driven by a few dust events, which the model reproduces (Figure S2). Black
 228 carbon and sea salt (not shown) make only minor contributions to aerosol mass. The model underestimates sulfate
 229 by 28% in the PBL, which leads to a 20% overestimate of nitrate, with canceling effect on the SNA mass simulation.

230 The GEOS-Chem simulation of organic aerosol in this work uses the simple scheme of Pai et al. (2020) and
 231 underestimates aircraft observations by 16% in the PBL. Over 90% of GEOS-Chem organic aerosol is secondary,
 232 consistent with observations (Figure S4; Nault et al., 2018; Pai et al., 2020). GEOS-Chem simulation of the
 233 KORUS-AQ aerosol component profiles for different meteorological regimes is presented in Park et al. (2021).



234
 235 **Figure 1. Vertical profiles of aerosol mass during KORUS-AQ.** Panel (a) shows the mean vertical distributions of
 236 observed mass concentrations of major aerosol components at ambient temperature and pressure. Panel (b) is the same as
 237 (a) but from the GEOS-Chem model sampled along the flight tracks (inset). We derive dust concentration from SAGA
 238 Ca²⁺ and Na⁺ following Shah et al. (2020) by assuming that non-sea salt Ca²⁺ accounts for 7.1% of dust mass: [dust] =
 239 $([Ca^{2+}] - 0.0439 [Na^+]/2) / 0.071$ where the brackets denote mass concentration. Modeled dust is shown for particles with
 240 geometric diameter < 2.5 µm, to be consistent with SAGA measurements (Table 2 footnote e). Measured sulfate, nitrate,
 241 ammonium, and organic aerosol concentrations are from the AMS instrument (values from the SAGA instrument are
 242 shown in Figure S4). All data are averaged over 500-m vertical bins. Here and elsewhere, we excluded pollution plumes
 243 diagnosed by either NO₂ or SO₂ > 10 ppbv (3.4% of all the data).

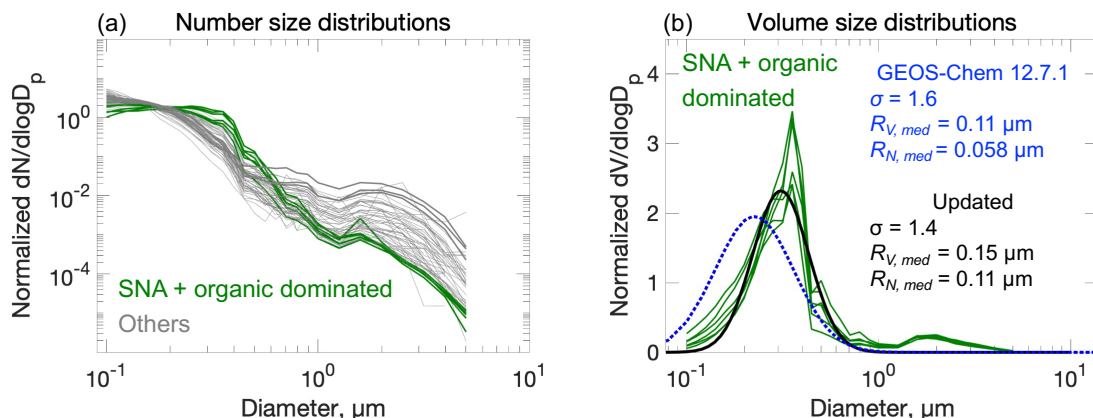
244 **3.2 Aerosol size distributions**

245 Figure 2a shows the normalized dry aerosol number size distributions on each of the 20 flights and in 3 altitude
246 bands: < 1.5 km, 3-5 km, and 6-7 km (60 lines). The spread in the size distributions above 1 μm in diameter reflects
247 dust influence. We select measurements below 1.5 km altitude when SNA + organic aerosol mass concentrations are
248 more than 4 times that of dust as defining the SNA + organic aerosol size distributions (green lines in Figure 2a).
249 Conditions dominated by SNA + organic aerosols define the lower envelopes of the ensemble of size distributions at
250 diameter > 1 μm . SNA and organics were observed to have similar size distributions during KORUS-AQ (Kim et
251 al., 2018).

252 Figure 2b converts the SNA + organic dominated number size distributions to volume size distributions. The
253 observed SNA + organic dominated aerosol size distribution is shifted toward larger sizes relative to the standard
254 GEOS-Chem. The secondary maximum in the coarse mode could be due to dust. We fitted the observed SNA +
255 organic aerosol size distributions to a lognormal distribution with volume median radius $R_{V,med} = 0.15 \mu\text{m}$ and
256 geometric standard deviation $\sigma = 1.4$. The number median radius is derived from the volume median radius
257 following Seinfeld and Pandis (2016):

258
$$\ln R_{N,med} = \ln R_{V,med} - 3\ln^2\sigma \quad (1)$$

259 which yields $R_{N,med} = 0.11 \mu\text{m}$. In comparison, the standard GEOS-Chem size distribution from Latimer and Martin
260 (2019) has $R_{N,med} = 0.058 \mu\text{m}$ and $\sigma = 1.6$. We adopt the observed log-normal size distribution parameters in what
261 follows (Table 3).



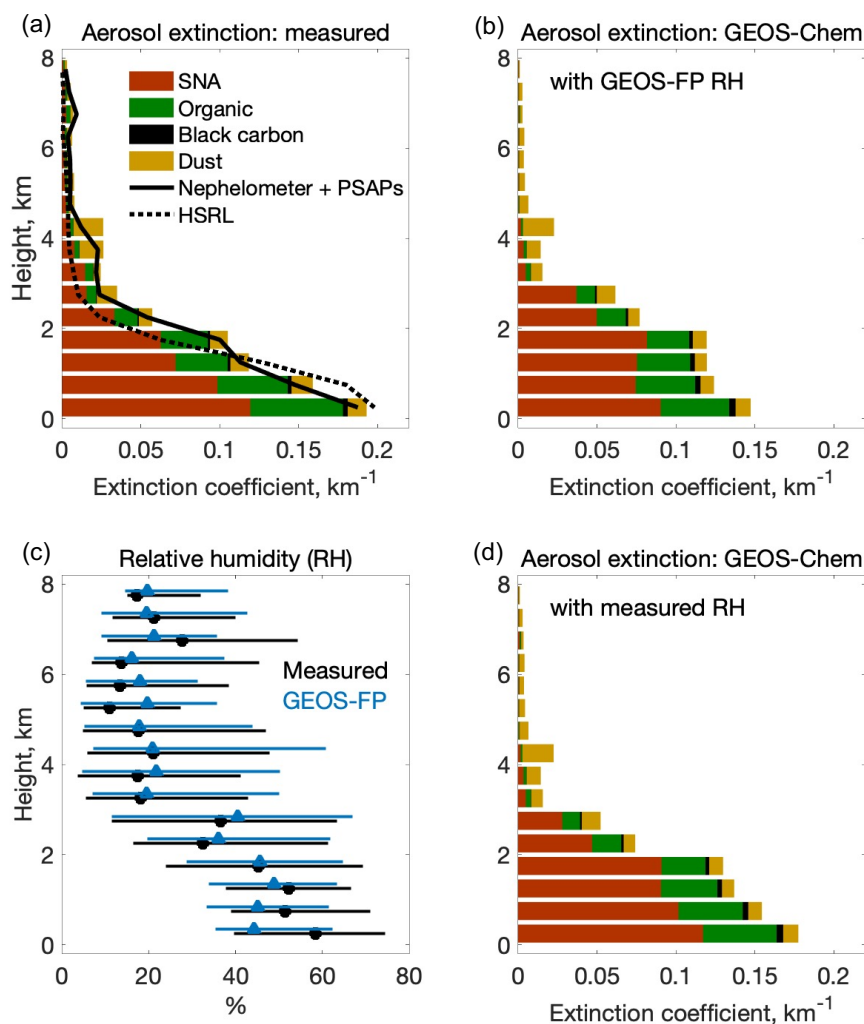
263
 264 **Figure 2. Aerosol dry size distributions measured in the KORUS-AQ aircraft campaign. Panel (a) shows mean**
 265 **normalized number size distributions measured on each of the 20 flights and for 3 altitude bins: < 1.5 km, 3-5 km, and 6-7**
 266 **km (60 lines total). The SNA + organic dominated size distribution profiles are highlighted in color. Panel (b) shows**
 267 **normalized volume size distributions for conditions dominated by SNA + organic aerosols (green lines), along with a least-**
 268 **square fit to a lognormal distribution (black line), and the standard GEOS-Chem v12.7.1 size distribution from Latimer**
 269 **and Martin (2019) (blue dashed line). Normalization imposes an arbitrary value of unit area below each line. Lognormal**
 270 **distribution parameters are inset in panel (b) including volume median radius ($R_{V,med}$), number median radius ($R_{N,med}$),**
 271 **and geometric standard deviation (σ).**

272 3.3 Aerosol extinction and relation to AOD

273 Figure 3 shows the vertical profiles of ambient aerosol extinction coefficients and RH during KORUS-AQ. Vertical
 274 profiles of aerosol extinction were measured on the aircraft both remotely with the HSRL instrument (above and
 275 below the aircraft) and in situ with TSI-3563 nephelometers (for scattering) and PSAPs (for absorption). The two
 276 agree well, as shown in Figure 3a. They indicate that 76-90% of column aerosol extinction is in the PBL at 0-2 km
 277 altitude and 9-19% is in the lower FT at 2-5 km. Both measurements show that aerosol extinction is much more
 278 strongly weighted to the PBL than aerosol mass (Figure 1).

279 Also shown in Figure 3a are the contributions of individual aerosol components to the extinction profile, as
 280 computed from the GEOS-Chem optical properties (Table 3) applied to the observed mass concentrations. The sum
 281 shows a good match to the measured extinction coefficient profiles. The much larger contribution of the PBL to
 282 column aerosol extinction than to column mass is because aerosol mass in the lower FT is mainly composed of dust,
 283 whose mass extinction efficiency is much smaller than SNA and organics due to its coarse size and lack of
 284 hygroscopic growth (Figure S5). The mean AOD inferred from the aircraft data is 0.36 and is contributed 59% by
 285 SNA, 27% by organic aerosol, 12% by dust, and 2% by BC. It is consistent with the mean AODs measured at
 286 AERONET stations in South Korea during KORUS-AQ (Figure S6).

287 Figure 3b shows the GEOS-Chem simulation of aerosol extinction profiles for comparison to the observations in
 288 Figure 3a. The model underestimates extinction coefficients by 20% below 1 km altitude, leading to a 10%
 289 underestimate of aircraft inferred AOD, although there is no such underestimate in aerosol mass. This is caused by a
 290 negative RH bias in the GEOS-FP meteorological data used to drive GEOS-Chem, particularly at high RH
 291 conditions (Figure 3c) and is corrected if we apply the observed RH rather than the GEOS-FP RH to the GEOS-
 292 Chem aerosol mass concentrations (Figure 3d).



293
 294 **Figure 3. Vertical profiles of aerosol extinction coefficients and relative humidity (RH) during KORUS-AQ. Panel (a)**
 295 **shows the mean observed vertical distributions of 550 nm extinction coefficients measured in situ (nephelometer + PSAPs;**
 296 **at ambient RH) and remotely (HSRL), along with an independent calculation (colored horizontal bars) from the**
 297 **measured mass concentrations of major aerosol components, measured RH, and GEOS-Chem optical properties as given**
 298 **in Table 3. Panel (b) shows the mean aerosol extinction profile in GEOS-Chem and the contributions from the different**
 299 **model components. Panel (c) is the median vertical profile of RH (horizontal bars are 25-75th percentiles) from aircraft**
 300 **measurements and the GEOS-FP assimilated meteorological data used to drive GEOS-Chem. Panel (d) is the same as (b)**
 301 **but calculated using measured RH.**

302 4 AOD and surface particulate matter over South Korea during KORUS-AQ

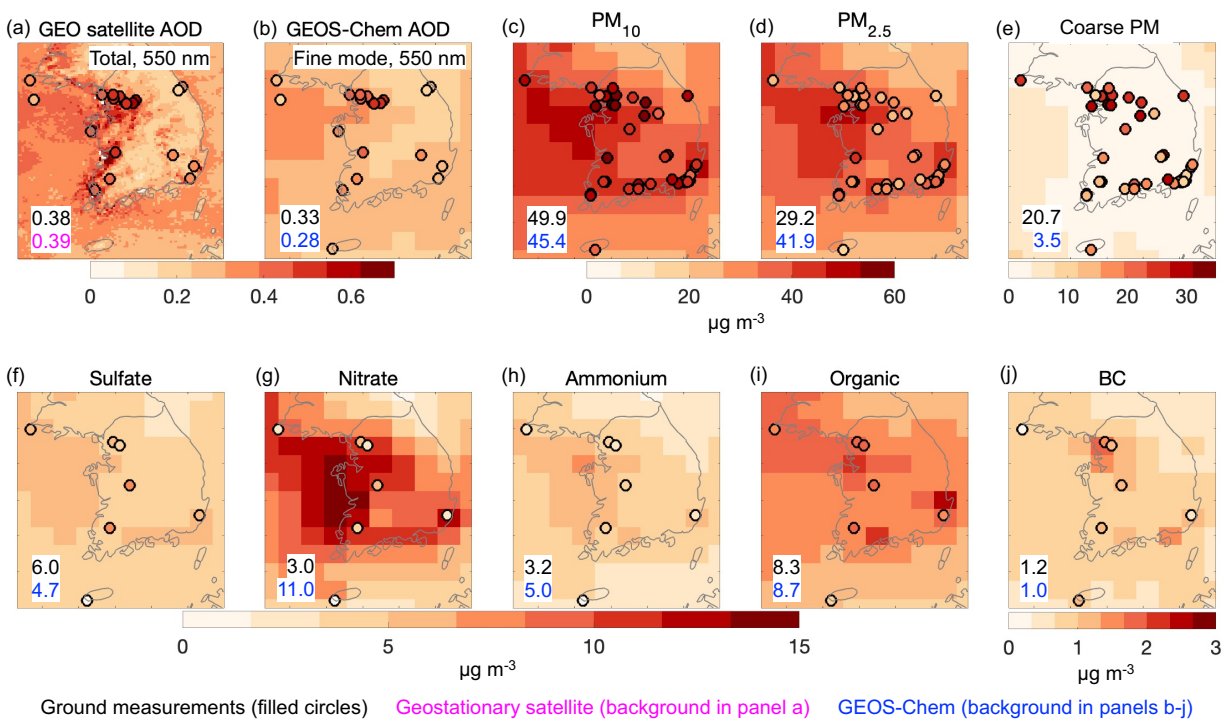
303 Our analysis of Section 3 used the KORUS-AQ aircraft data together with GEOS-Chem to attribute AOD over
304 South Korea to individual aerosol components and altitudes. We now take the next step of evaluating the capability
305 of GEOS-Chem to independently simulate observed AODs and surface particulate matter concentrations.

306 Figure 4a shows the spatial distribution of the fused geostationary satellite (GOCI/AHI) AOD (GEO satellite AOD)
307 during the KORUS-AQ period with AERONET total AOD added as circles. The GEO satellite AOD shows high
308 values (0.5-0.6) along the west coast of South Korea, significantly correlated with AERONET total AOD with a
309 spatial correlation coefficient (R) of 0.7. GEO satellite AOD is biased low at sites in the Seoul Metropolitan Area
310 (SMA) and is biased high on the Yellow Sea islands, resulting in an overall -10% bias. The low biases in the SMA
311 could be due to high-concentration aerosol pixels mis-identified as clouds and/or possible issues with the aerosol
312 type assumption in the aerosol retrieval, while the high biases on the Yellow Sea islands could result from
313 uncertainties in the assumption of ocean surface reflectance, as has been discussed by Choi et al. (2016, 2018) and
314 Lim et al. (2018, 2021). Sampling the AODs at or near the seven PM_{2.5} supersites operating during KORUS-AQ
315 shows no significant bias (inset values in Figure 4a).

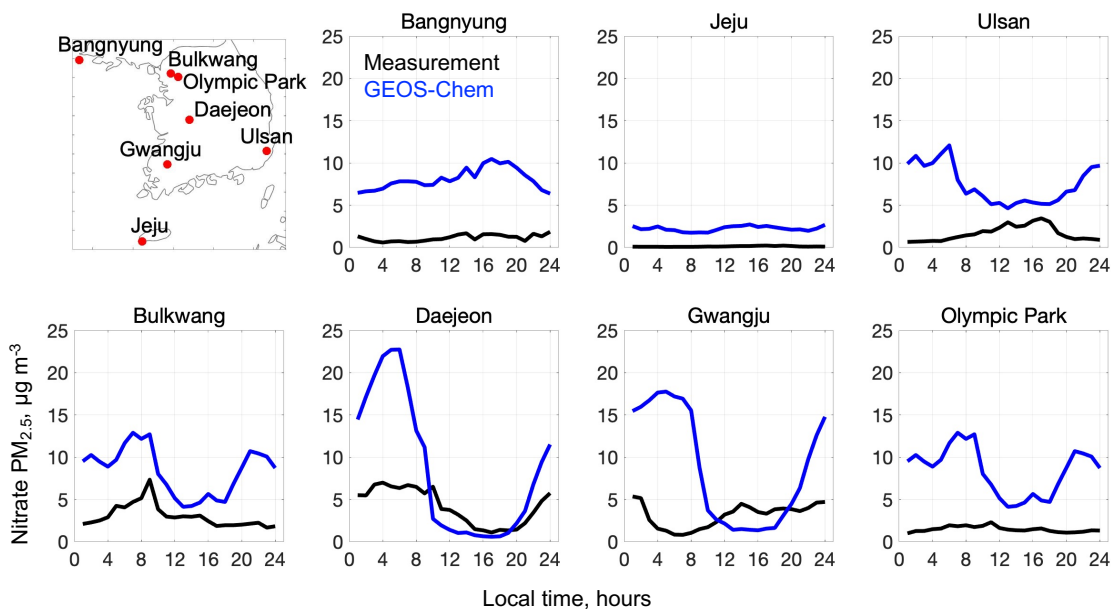
316 Figure 4b-e shows the spatial distributions of GEOS-Chem AOD, surface PM₁₀ (particulate matter with aerodynamic
317 diameter less than 10 μm), surface PM_{2.5}, and surface coarse PM (PM₁₀ minus PM_{2.5}; particulate matter with
318 aerodynamic diameter less than 10 μm and larger than 2.5 μm), with surface observations shown as circles and
319 median values at the measurement sites inset. GEOS-Chem reproduces the satellite AOD enhancements along the
320 west coast of South Korea but the values are lower than observed, which we attribute to unaccounted coarse PM and
321 negative RH bias as discussed below. Comparison of AERONET total and fine mode AOD shows a 13%
322 contribution of coarse particles to total AOD. Comparison of GEOS-Chem to the fine-mode AERONET AOD, as
323 shown in Figure 4b, finds a 15% underestimate that could be attributed to the low-RH bias (Figure 3c). Concurrent
324 measurements of PM₁₀ and PM_{2.5} at AirKorea sites show that coarse PM (median 21 $\mu\text{g m}^{-3}$) accounts for 41% of
325 total PM₁₀ (50 $\mu\text{g m}^{-3}$), while coarse PM in GEOS-Chem is much lower (3.5 $\mu\text{g m}^{-3}$; Figure 4e). Therefore, about
326 half of the GEOS-Chem underestimate of total AOD can be attributed to missing coarse PM, with the other half
327 comes from negative RH bias. Coarse PM has a concentration larger than 10 $\mu\text{g m}^{-3}$ across South Korea, with higher
328 concentration in the SMA ($\sim 30 \mu\text{g m}^{-3}$) than in rural areas ($\sim 15 \mu\text{g m}^{-3}$), implying an origin from both
329 anthropogenic and natural sources (Figure 4e).

330 GEOS-Chem overestimates surface PM_{2.5} by 43% over South Korea (Figure 4d), in contrast to the simulation of
331 AERONET fine mode AOD (Figure 4b). Figure 4f-j shows the spatial distributions of major PM_{2.5} components in
332 GEOS-Chem (background) and measurements (filled circles). GEOS-Chem is not significantly biased relative to the
333 observations for organic aerosol and BC, and underestimates sulfate by 22%. We find that the model bias for PM_{2.5}
334 is largely driven by nitrate, which is overestimated by a factor of 3 and leads to a 56% overestimate of ammonium.
335 By contrast, comparison to the KORUS-AQ data below 1-km altitude showed only a 20% overestimate of nitrate
336 (Figure 1). This is because the model bias is mainly driven by nighttime conditions (Figure 5), while aircraft

337 samples in the daytime during KORUS-AQ. The cause of this large model bias is analyzed by K. R. Travis et al.
 338 (manuscript in preparation) and is attributed to nighttime nitrate chemistry and deposition in the stratified boundary
 339 layer.



340
 341 **Figure 4.** Spatial distributions of AOD and surface PM_{10} , $PM_{2.5}$, coarse PM (PM_{10} minus $PM_{2.5}$), and major $PM_{2.5}$
 342 components over South Korea averaged during KORUS-AQ (May 9 - June 10, 2016). Panel (a) shows the fused
 343 geostationary (GEO) 550 nm AOD from the GOCI and AHI satellites (background) and AERONET 550 nm total AOD
 344 (filled circles). Panel (b) shows GEOS-Chem 550 nm AOD sampled at hourly GEO satellite AOD (GEOS-Chem clear-sky
 345 AOD; background) and AERONET 550 nm fine mode AOD (filled circles). Panel (c) shows surface PM_{10} modelled by
 346 GEOS-Chem (background) and measured at ground sites (filled circles). Panels (d-j) are the same as panel (c) but
 347 respectively for $PM_{2.5}$, coarse PM (PM_{10} minus $PM_{2.5}$), and sulfate, nitrate, ammonium, organic, and BC $PM_{2.5}$
 348 components. Values inset are median values from ground-based measurements (black) and sampled from GEO satellite
 349 (magenta) and GEOS-Chem (blue). Measured PM_{10} , $PM_{2.5}$, and coarse PM in panels (c-e) are shown for a random
 350 selection of 50% of AirKorea sites to visualize spatial distribution, and inset values are for the seven supersites where
 351 $PM_{2.5}$ composition was measured. Median AOD values inset are sampled at or near the seven supersites to avoid biasing
 352 by the large number of sites in the Seoul Metropolitan Area. Modelled total $PM_{2.5}$ concentrations are calculated at 35%
 353 RH (Table 3). Modelled PM_{10} is the sum of $PM_{2.5}$, coarse dust, and coarse sea salt.



354
 355 **Figure 5. Median diurnal variations of PM_{2.5} nitrate concentrations at the seven supersites (top left panel) operated in**
 356 **South Korea during KORUS-AQ (May 9 - June 10, 2016). Values are medians binned by hour. GEOS-Chem model**
 357 **values are sampled to coincide with the measurements.**

358 5 AOD and its relationship to PM_{2.5} over East Asia

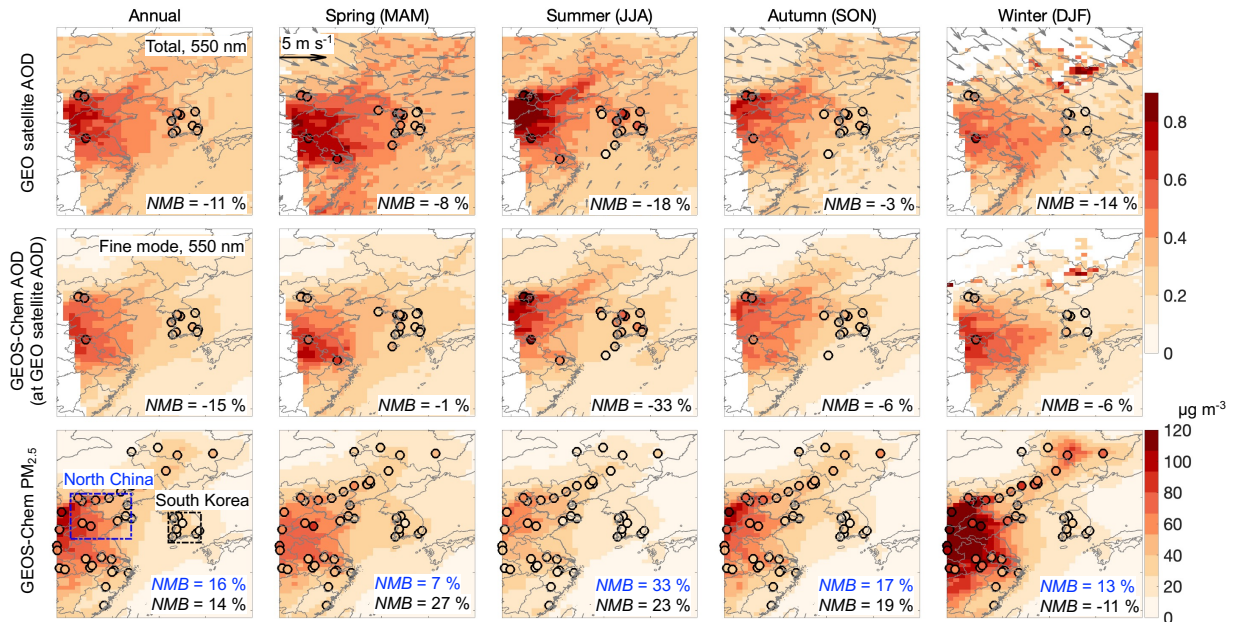
359 We build on our analysis of the KORUS-AQ period for a broader interpretation of the distribution of AOD over
 360 Korea and China and its relationship to surface PM_{2.5}, acknowledging that the conditions sampled in KORUS-AQ
 361 may not be representative of other seasons or of China. Figure 6 shows the spatial distributions of 2016 annual and
 362 seasonal mean geostationary (GEO) satellite AODs, the corresponding GEOS-Chem clear-sky AODs, and GEOS-
 363 Chem surface PM_{2.5}. The Figure gives normalized mean biases (*NMBs*) relative to ground-based measurements from
 364 AERONET and from the PM_{2.5} surface networks (shown as circles) over the North China region (115.5-122° E,
 365 34.5-40.5° N) and South Korea. The North China region is defined to overlap with the domain of the geostationary
 366 satellite AOD, and to ensure consistent seasonal variations within its narrow latitude.

367 On an annual mean basis, AOD over North China (~ 0.5-0.6) is about 50% larger than over South Korea (~ 0.3-0.4).
 368 AOD over South Korea shows higher values (> 0.4) in the Seoul Metropolitan Area, consistent with that during the
 369 KORUS-AQ period (Figure 4a). Transport from the Asian continent is strongest in spring when the frequency of
 370 cold front passages is highest (Liu et al., 2003). AERONET total AOD in spring (0.4-0.6) is twice as large as fine-
 371 mode AOD (0.2-0.3), reflecting a large contribution of dust. In seasons other than spring, 80-90% of AERONET
 372 total AOD is contributed by the fine mode. There is large seasonality in AODs over North China, and weaker
 373 seasonality over South Korea, which will be discussed below.

374 The GEOS-Chem clear-sky AODs show the same spatial and seasonal patterns as GEO satellite AODs but tend to
 375 be low in spring and summer. Comparison of the model to AERONET AODs confirms this bias and shows better

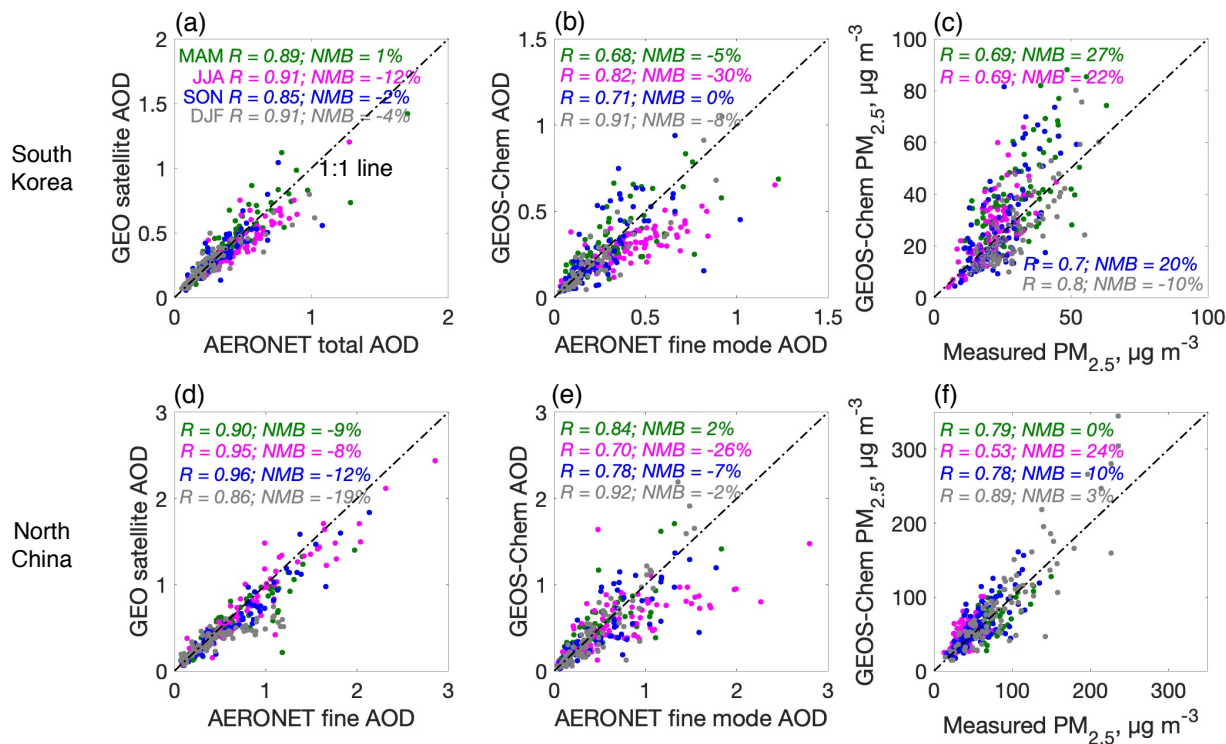
376 agreement with fine-mode AOD in spring (*NMB* of -1%), implying an underestimate of coarse dust that is consistent
377 with our comparisons to the AirKorea network data (Figure 4e). Comparison of clear-sky and all-sky AODs in
378 GEOS-Chem shows no significant difference on an annual and seasonal mean basis, except for winter (Figure S7).
379 Winter has larger all-sky AOD than clear-sky AOD and the lowest rate of successful satellite retrievals (Figure S7),
380 which may be due in part to misclassification of heavy wintertime $PM_{2.5}$ pollution as clouds (Zhang et al., 2020).

381 The spatial distributions of $PM_{2.5}$ in GEOS-Chem in different seasons match closely the observations (Figure 6,
382 bottom row). We see also a close coincidence between the spatial distributions of $PM_{2.5}$ and AODs, both in the
383 observations and the model. On an annual mean basis, GEOS-Chem overestimates $PM_{2.5}$ by 16% in North China
384 and by 14% in South Korea, even though it underestimates AERONET fine mode AODs by 15%. The overestimate
385 of $PM_{2.5}$ in South Korea is worst in spring (27%), consistent with KORUS-AQ results which we previously
386 attributed to excessive nighttime nitrate build-up in the model. Over North China, the overestimate of $PM_{2.5}$ is worst
387 in summer (33%), consistent with the nitrate overestimate in summer shown in our previous study (Zhai et al.,
388 2021), which could also be due to model overestimate of nighttime nitrate (Miao et al., 2020).



389
 390 **Figure 6. Spatial distributions of 2016 annual and seasonal mean AOD (550 nm) and surface PM_{2.5}. The top row shows**
 391 **the observed GOCI/AHI geostationary satellite AOD (GEO satellite AOD) on the GEOS-Chem $0.5^\circ \times 0.625^\circ$ grid with**
 392 **superimposed 925 hPa GEOS-FP wind fields and AERONET total AODs (circles). The middle row shows clear-sky**
 393 **GEOS-Chem AOD, with AERONET fine mode AOD added as circles. The bottom row shows GEOS-Chem surface PM_{2.5}**
 394 **(background) with surface network measurements (circles). AERONET AODs are shown only when more than 10**
 395 **months of data are available for the annual mean and all 3 months data are available for each season. The PM_{2.5}**
 396 **observations shown are for a random selection of 7% of network sites for visual clarity. GEOS-Chem PM_{2.5} is calculated**
 397 **at 35% RH (Table 3). Normalized mean biases (NMBs) inset are for the comparisons of GEO satellite and GEOS-Chem**
 398 **values to the corresponding ground measurements.**

399
 400 Figure 7 shows daily correlations of the regional average series between AERONET total AOD and GEO satellite
 401 AOD, between AERONET fine mode AOD and GEOS-Chem AOD, as well as between measured PM_{2.5} and GEOS-
 402 Chem PM_{2.5}. Correlations in Figure 7 are all statistically significant with correlation coefficients (*R*) ranging from
 403 around 0.7 to more than 0.9 and normalized mean biases (*NMB*) within $\pm 30\%$. The correlations of these three pairs
 404 are similar over South Korea and North China, except that GEOS-Chem overestimates springtime PM_{2.5} in South
 405 Korea but not over North China, possibly due to a model overestimate of the long-range transport of PM_{2.5} from
 406 China to South Korea in spring.

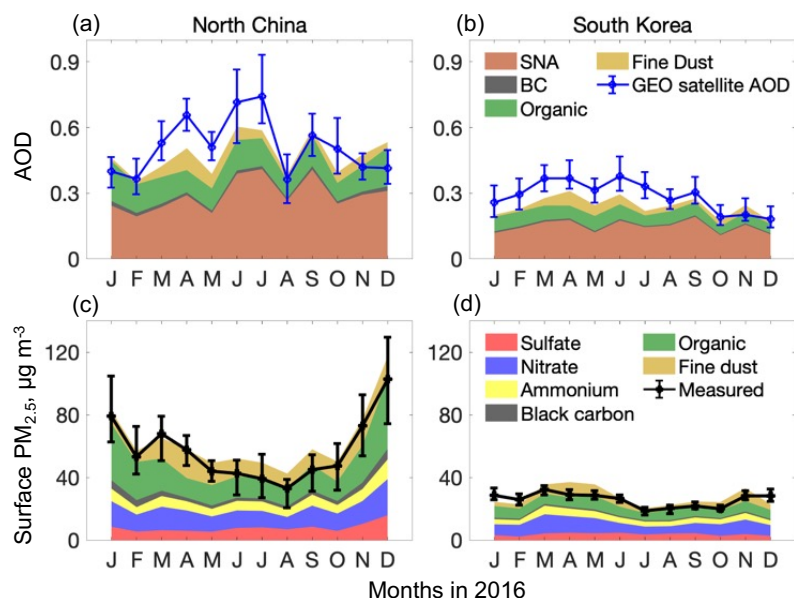


407
 408 **Figure 7. Scatter plots of regional mean daily (a and d) GEO satellite AOD vs. AERONET total AOD, (b and e) GEOS-**
 409 **Chem AOD vs. AERONET fine-model AOD, and (c and f) GEOS-Chem PM_{2.5} vs. measured PM_{2.5} over South Korea (a-c)**
 410 **and North China (d-f). Different colors represent different seasons. Values inset are correlation coefficients (*R*) and**
 411 **normalized mean biases (*NMB*) between surface measurements and GEO satellite or GEOS-Chem values.**

412
 413 Figure 8 compares the seasonalities of AOD and PM_{2.5} over the North China and South Korea regions. The GEO
 414 satellite AOD over North China peaks in July and is minimum in winter. Most of AOD is attributed by GEOS-Chem
 415 to SNA aerosol, same as in South Korea. AOD over South Korea also has a summer maximum and winter minimum
 416 but with weaker amplitude than over North China. The GEOS-Chem AOD is ~20% biased low in summer and this
 417 is largely due to a low RH bias (Figure S8), as seen previously in the KORUS-AQ comparisons but amplified by the
 418 high RH in summer that drives hygroscopic growth (Latimer and Martin, 2019).

419 Surface PM_{2.5} in the observations over North China and South Korea shows opposite seasonality to AOD, with
 420 minimum values in summer and maximum values in winter-spring. GEOS-Chem reproduces the strong seasonality
 421 of PM_{2.5} in North China and the much weaker seasonality in South Korea. The high PM_{2.5} values over North China
 422 in winter in the model are mostly driven by organic aerosol, reflecting the large residential coal burning source
 423 (Figure S9; Zheng et al., 2018). In South Korea, by contrast, household energy is mainly from natural gas and
 424 electricity (Lee et al., 2020; Woo et al., 2020). GEOS-FP daytime PBL height also shows a stronger seasonality over
 425 North China than over South Korea (Figure S8), generally consistent with the CALIPSO daytime PBL height (Su et
 426 al., 2018). Previous studies have shown opposite seasonality between MODIS AOD and surface PM_{2.5} over North

427 China and attributed this to the seasonality in PBL height and RH (Qu et al., 2016; Xu et al., 2019). The mean
 428 $PM_{2.5}/AOD$ ratio over North China in winter ($236 \mu g m^{-3}$) is 8 times that in summer ($29 \mu g m^{-3}$), with autumn ($94 \mu g$
 429 m^{-3}) and spring ($89 \mu g m^{-3}$) in between, while over South Korea, the $PM_{2.5}/AOD$ ratio in winter ($62 \mu g m^{-3}$) is only
 430 70% larger than in summer ($36 \mu g m^{-3}$).



431
 432 **Figure 8. Seasonality of AOD and $PM_{2.5}$ over North China and South Korea, and contributions from individual aerosol**
 433 **components. Lines show regional medians (error bars: 25th and 75th percentiles) for the ensemble of monthly averaged**
 434 **observations in the regions (Figure 6) in 2016. GEOS-Chem values are shown as stacked contours for individual**
 435 **components and are sampled in the same way as the observations.**

436 6 Conclusions

437 Geostationary satellite observations of aerosol optical depth (AOD) over East Asia may usefully complement $PM_{2.5}$
 438 air quality networks if the local relationship between AOD and $PM_{2.5}$ can be inferred from a physical and/or
 439 statistical model. Here we analyzed the ability of the GEOS-Chem chemical transport model to provide this
 440 relationship by using a new fused GOCI/AHI geostationary satellite product together with AERONET ground-based
 441 AOD measurements, aerosol vertical profiles over South Korea from the KORUS-AQ aircraft campaign (May-June
 442 2016), and surface network observations. This allowed us to identify the critical features and limitations of the
 443 model for successful representing the AOD- $PM_{2.5}$ relationship.

444 The KORUS-AQ observations show that total aerosol extinction (550 nm) in the vertical column is dominated by
 445 sulfate-nitrate-ammonium (SNA) and organic aerosol in the planetary boundary layer (PBL), despite large
 446 concentrations of dust in the free troposphere. This reflects the optically effective size and high hygroscopicity of
 447 the PBL aerosols. We find that GEOS-Chem aerosol optical properties based on measurements over the North
 448 America (default model setting) underestimate KORUS-AQ aerosol mass extinction efficiency by around 20%. In

449 addition, a low bias in GEOS-FP RH below 1 km leads to a 10% underestimate of AOD inferred from the aircraft
450 profile. Adjustments of GEOS-Chem aerosol optical properties and RH enable a successful simulation of the aerosol
451 extinction profile. SNA aerosol contributes 59% of column aerosol extinction in the KORUS-AQ data, while
452 organic aerosol contributes 27% and dust contributes 12%.

453 Comparison of GOCI/AHI geostationary (GEO) satellite AOD to AERONET AODs over South Korea shows good
454 agreement, with high values along the west coast. GEOS-Chem is more consistent with the fine-mode AERONET
455 AOD because of its insufficient accounting of coarse particles, which account for 13% of AERONET AOD. The
456 remaining 15% underestimate of AERONET fine-mode AOD by GEOS-Chem can be attributed to the RH low bias.
457 GEOS-Chem overestimates 24-h surface $PM_{2.5}$ over South Korea by 43% during the KORUS-AQ period, despite its
458 successful simulation of the aircraft data and fine-mode AERONET AOD, and we find that this is due to a large
459 overestimate of nighttime nitrate.

460 Broader examination of the GOCI/AHI AOD satellite data over East Asia shows spatial distributions and
461 magnitudes consistent with AERONET and featuring in particular strong Asian outflow in spring that includes a
462 large dust component. We find that AODs and $PM_{2.5}$ have similar large-scale spatial distributions but opposite
463 seasonality. $PM_{2.5}$ in North China has a strong winter maximum and summer minimum, while AOD shows the
464 opposite. GEOS-Chem simulates successfully the seasonality of measured $PM_{2.5}$ but is ~ 20% biased low in summer
465 for AOD, due again to RH low bias like that during KORUS-AQ, amplified by the high RH in summer that drives
466 hygroscopic growth (Latimer and Martin, 2019). We find that the opposite AOD and $PM_{2.5}$ seasonality is mainly
467 driven by residential coal heating sources and low PBL depths in winter, and high RH in summer. Observations of
468 $PM_{2.5}$ and AOD in South Korea show the same seasonal phases as in North China but with much weaker amplitude,
469 reflecting the lack of residential coal burning in winter and a weaker seasonal amplitude of PBL depth.

470 In summary, we find that the geostationary GOCI/AHI satellite AOD data provide high-quality information for
471 monitoring of $PM_{2.5}$ over East Asia but that physical interpretation requires accurate information on aerosol size
472 distributions, PBL depths, RH, the role of coarse particles, and diurnal variation of $PM_{2.5}$, all of which are subject to
473 large uncertainties in chemical transport models. Addressing these uncertainties should be a target of future work.
474 We have used results from our study in a recent machine-learning reconstruction of daily 2011-present $PM_{2.5}$ over
475 East Asia from GOCI AOD data by identifying critical variables for the machine-learning algorithm and providing
476 blended gap-filling data for cloudy scenes (Pendergrass et al., 2021). Besides the factors discussed in this study,
477 topography might be another important factor influencing surface $PM_{2.5}$ and its vertical mixing (Su et al., 2018), and
478 this also requires future investigation.

479

480 *Data availability.* Aircraft data during KORUS-AQ are available at: [www-air.larc.nasa.gov/cgi-](http://www-air.larc.nasa.gov/cgi-bin/ArcView/korusaq)
481 [bin/ArcView/korusaq](http://www-air.larc.nasa.gov/cgi-bin/ArcView/korusaq). $PM_{2.5}$ data over China are from: quotsoft.net/air/. $PM_{2.5}$ data over South Korea are from:
482 www.airkorea.or.kr/web. AERONET data can be found at: aeronet.gsfc.nasa.gov. The MEIC emission inventory are

483 at: www.meicmodel.org/. The KORUSv5 emission inventory is developed by Konkuk University, available at:
484 http://aisl.konkuk.ac.kr/#/emission_data/korus-aq_emissions.

485
486 *Author contributions.* SZ and DJJ designed the study. SZ performed the data analysis and model simulations with
487 contributions from JFB, KL, HCL, SKK, XW, PL, KRT, and Hong Liao. JK, SL, and Hyunkwang Lim provided
488 satellite AOD data. RJP and JIJ contributed to AirKorea data processing. JM and RM provided the dust emission
489 inventory. GL, FY, and JMM updated wet deposition simulation. JWH, BEA, JED, JLJ, PCJ, and BAN contributed
490 to KORUS-AQ campaign measurements. JHW and YK provided the KORUSv5 emission inventory. QZ provided
491 the MEIC emission inventory. SZ and DJJ wrote the paper with input from all authors.

492
493 *Acknowledgement.* This work was funded by the Samsung Advanced Institute of Technology and the Harvard-
494 NUIST Joint Laboratory for Air Quality and Climate (JLAQC). JLJ, PCJ, and BAN acknowledge NASA grant
495 NNX15AT96G and 80NSSC19K0124 for support.

496
497 *Competing interests.* The authors declare that they have no conflict of interest.

498

499 **References**

- 500 Alexander, B., Park Rokjin, J., Jacob Daniel, J., and Gong, S.: Transition metal-catalyzed oxidation of atmospheric
501 sulfur: Global implications for the sulfur budget, *J. Geophys. Res. Atmos.*, 114, D02309,
502 <https://doi.org/10.1029/2008JD010486>, 2009.
- 503 Amos, H. M., Jacob, D. J., Holmes, C. D., Fisher, J. A., Wang, Q., Yantosca, R. M., Corbitt, E. S., Galarneau, E.,
504 Rutter, A. P., Gustin, M. S., Steffen, A., Schauer, J. J., Graydon, J. A., Louis, V. L. S., Talbot, R. W., Edgerton, E.
505 S., Zhang, Y., and Sunderland, E. M.: Gas-particle partitioning of atmospheric Hg(II) and its effect on global
506 mercury deposition, *Atmos. Chem. Phys.*, 12, 591-603, <https://doi.org/10.5194/acp-12-591-2012>, 2012.
- 507 Brauer, M., Freedman, G., Frostad, J., van Donkelaar, A., Martin, R. V., Dentener, F., Dingenen, R. v., Estep, K.,
508 Amini, H., Apte, J. S., Balakrishnan, K., Barregard, L., Broday, D., Feigin, V., Ghosh, S., Hopke, P. K., Knibbs, L.
509 D., Kokubo, Y., Liu, Y., Ma, S., Morawska, L., Sangrador, J. L. T., Shaddick, G., Anderson, H. R., Vos, T.,
510 Forouzanfar, M. H., Burnett, R. T., and Cohen, A.: Ambient Air Pollution Exposure Estimation for the Global
511 Burden of Disease 2013, *Environ. Sci. Technol.*, 50, 79-88, [10.1021/acs.est.5b03709](https://doi.org/10.1021/acs.est.5b03709), 2016.
- 512 Brock, C. A., Wagner, N. L., Anderson, B. E., Beyersdorf, A., Campuzano-Jost, P., Day, D. A., Diskin, G. S.,
513 Gordon, T. D., Jimenez, J. L., Lack, D. A., Liao, J., Markovic, M. Z., Middlebrook, A. M., Perring, A. E.,
514 Richardson, M. S., Schwarz, J. P., Welti, A., Ziemba, L. D., and Murphy, D. M.: Aerosol optical properties in the
515 southeastern United States in summer – Part 2: Sensitivity of aerosol optical depth to relative humidity and aerosol
516 parameters, *Atmos. Chem. Phys.*, 16, 5009-5019, [10.5194/acp-16-5009-2016](https://doi.org/10.5194/acp-16-5009-2016), 2016.
- 517 Chen, G., Li, S., Knibbs, L. D., Hamm, N. A. S., Cao, W., Li, T., Guo, J., Ren, H., Abramson, M. J., and Guo, Y.: A
518 machine learning method to estimate PM_{2.5} concentrations across China with remote sensing, meteorological and
519 land use information, *Sci. Total Environ.*, 636, 52-60, <https://doi.org/10.1016/j.scitotenv.2018.04.251>, 2018.

520 Chen, W., Tang, H., and Zhao, H.: Diurnal, weekly and monthly spatial variations of air pollutants and air quality of
521 Beijing, *Atmos. Environ.*, 119, 21-34, <https://doi.org/10.1016/j.atmosenv.2015.08.040>, 2015.

522 Chen, J., Yin, J., Zang, L., Zhang, T., and Zhao, M.: Stacking machine learning model for estimating hourly PM_{2.5} in
523 China based on Himawari 8 aerosol optical depth data, *Sci. Total Environ*, 697, 134021,
524 <https://doi.org/10.1016/j.scitotenv.2019.134021>, 2019.

525 Cheng, Y., Dai, T., Goto, D., Schutgens, N. A. J., Shi, G., and Nakajima, T.: Investigating the assimilation of
526 CALIPSO global aerosol vertical observations using a four-dimensional ensemble Kalman filter, *Atmos. Chem.
527 Phys.*, 19, 13445-13467, <https://doi.org/10.5194/acp-19-13445-2019>, 2019.

528 Chin, M., Ginoux, P., Kinne, S., Torres, O., Holben, B. N., Duncan, B. N., Martin, R. V., Logan, J. A., Higurashi,
529 A., and Nakajima, T.: Tropospheric Aerosol Optical Thickness from the GOCART Model and Comparisons with
530 Satellite and Sun Photometer Measurements, *J. Atmos. Sci.*, 59, 461-483, [https://doi.org/10.1175/1520-0469\(2002\)059<0461:TAOTFT>2.0.CO;2](https://doi.org/10.1175/1520-0469(2002)059<0461:TAOTFT>2.0.CO;2), 2002.

532 Choi, M., Kim, J., Lee, J., Kim, M., Park, Y. J., Holben, B., Eck, T. F., Li, Z., and Song, C. H.: GOCI Yonsei
533 aerosol retrieval version 2 products: an improved algorithm and error analysis with uncertainty estimation from 5-
534 year validation over East Asia, *Atmos. Meas. Tech.*, 11, 385-408, [10.5194/amt-11-385-2018](https://doi.org/10.5194/amt-11-385-2018), 2018.

535 Choi, J., Park, R. J., Lee, H.-M., Lee, S., Jo, D. S., Jeong, J. I., Henze, D. K., Woo, J.-H., Ban, S.-J., Lee, M.-D.,
536 Lim, C.-S., Park, M.-K., Shin, H. J., Cho, S., Peterson, D., and Song, C.-K.: Impacts of local vs. trans-boundary
537 emissions from different sectors on PM_{2.5} exposure in South Korea during the KORUS-AQ campaign, *Atmos.
538 Environ.*, 203, 196-205, <https://doi.org/10.1016/j.atmosenv.2019.02.008>, 2019.

539 Choi, M., Kim, J., Lee, J., Kim, M., Park, Y. J., Jeong, U., Kim, W., Hong, H., Holben, B., Eck, T. F., Song, C. H.,
540 Lim, J. H., and Song, C. K.: GOCI Yonsei Aerosol Retrieval (YAER) algorithm and validation during the
541 DRAGON-NE Asia 2012 campaign, *Atmos. Meas. Tech.*, 9, 1377-1398, <https://doi.org/10.5194/amt-9-1377-2016>,
542 2016.

543 Crawford, J. H., Ahn, J. Y., Al-Saadi, J., Chang, L., Emmons, L., Kim, J., Lee, G., Park, J. H., Park, R., Woo, J. H.,
544 Song, C. K., Hong, J.-H., Hong, Y.-D., Lefer, B. L., Lee, M., Lee, T., Kim, S., Min, K.-E., Yum, S. S., Shin, H. J.,
545 Kim, Y.-W., Choi, J.-S., Park, J.-S., Szykman, J. J., Long, R. W., Jordan, C. E., Simpson, I. J., Fried, A., Dibb, J. E.,
546 Cho, S. Y., and Kim, Y. P.: The Korea-United States air quality (KORUS-AQ) field study, *Elementa-Sci. Anthropol.*,
547 in press, 2021.

548 Curci, G.: FlexAOD: a chemistry-transport model post-processing tool for a flexible calculation of aerosol optical
549 properties, 1-4, http://pumpkin.aquila.infn.it/gabri/download/curci_istp2012.pdf, 2012.

550 Dai, Q., Bi, X., Liu, B., Li, L., Ding, J., Song, W., Bi, S., Schulze, B. C., Song, C., Wu, J., Zhang, Y., Feng, Y., and
551 Hopke, P. K.: Chemical nature of PM_{2.5} and PM₁₀ in Xi'an, China: Insights into primary emissions and secondary
552 particle formation, *Environmental Pollution*, 240, 155-166, <https://doi.org/10.1016/j.envpol.2018.04.111>, 2018.

553 Di, Q., Amini, H., Shi, L., Kloog, I., Silvern, R., Kelly, J., Sabath, M. B., Choirat, C., Koutrakis, P., Lyapustin, A.,
554 Wang, Y., Mickley, L. J., and Schwartz, J.: An ensemble-based model of PM_{2.5} concentration across the contiguous
555 United States with high spatiotemporal resolution, *Environ. Int.*, 130, 104909,
556 <https://doi.org/10.1016/j.envint.2019.104909>, 2019.

557 Dibb, J. E., Talbot, R. W., Scheuer, E. M., Seid, G., Avery, M. A., and Singh, H. B.: Aerosol chemical composition
558 in Asian continental outflow during the TRACE-P campaign: Comparison with PEM-West B, *J. Geophys. Res.*
559 *Atmos.*, 108, 8815, <https://doi.org/10.1029/2002JD003111>, 2003.

560 Eck, T. F., Holben, B. N., Sinyuk, A., Pinker, R. T., Goloub, P., Chen, H., Chatenet, B., Li, Z., Singh, R. P.,
561 Tripathi, S. N., Reid, J. S., Giles, D. M., Dubovik, O., O'Neill, N. T., Smirnov, A., Wang, P., and Xia, X.:
562 Climatological aspects of the optical properties of fine/coarse mode aerosol mixtures, *J. Geophys. Res. Atmos.*, 115,
563 <https://doi.org/10.1029/2010JD014002>, 2010.

564 Fairlie, T. D., Jacob, D. J., and Park, R. J.: The impact of transpacific transport of mineral dust in the United States,
565 *Atmos. Environ.*, 41, 1251-1266, <https://doi.org/10.1016/j.atmosenv.2006.09.048>, 2007.

566 Fairlie, T. D., Jacob, D. J., Dibb, J. E., Alexander, B., Avery, M. A., van Donkelaar, A., and Zhang, L.: Impact of
567 mineral dust on nitrate, sulfate, and ozone in transpacific Asian pollution plumes, *Atmos. Chem. Phys.*, 10, 3999-
568 4012, <https://doi.org/10.5194/acp-10-3999-2010>, 2010.

569 Fisher, J. A., Jacob, D. J., Wang, Q., Bahreini, R., Carouge, C. C., Cubison, M. J., Dibb, J. E., Diehl, T., Jimenez, J.
570 L., Leibensperger, E. M., Lu, Z., Meinders, M. B. J., Pye, H. O. T., Quinn, P. K., Sharma, S., Streets, D. G., van
571 Donkelaar, A., and Yantosca, R. M.: Sources, distribution, and acidity of sulfate–ammonium aerosol in the Arctic in
572 winter–spring, *Atmos. Environ.*, 45, 7301–7318, <https://doi.org/10.1016/j.atmosenv.2011.08.030>, 2011.

573 Fountoukis, C. and Nenes, A.: ISORROPIA II: a computationally efficient thermodynamic equilibrium model for
574 $K^+Ca^{2+}Mg^{2+}NH_4^+Na^+SO_4^{2-}NO_3^-Cl^-H_2O$ aerosols, *Atmos. Chem. Phys.*, 7, 4639–4659,
575 <https://doi.org/10.5194/acp-7-4639-2007>, 2007.

576 Geng, G., Zhang, Q., Tong, D., Li, M., Zheng, Y., Wang, S., and He, K.: Chemical composition of ambient $PM_{2.5}$
577 over China and relationship to precursor emissions during 2005–2012, *Atmos. Chem. Phys.*, 17, 9187–9203,
578 <https://doi.org/10.5194/acp-17-9187-2017>, 2017.

579 Giles, D. M., Sinyuk, A., Sorokin, M. G., Schafer, J. S., Smirnov, A., Slutsker, I., Eck, T. F., Holben, B. N., Lewis,
580 J. R., Campbell, J. R., Welton, E. J., Korokin, S. V., and Lyapustin, A. I.: Advancements in the Aerosol Robotic
581 Network (AERONET) Version 3 database - automated near-real-time quality control algorithm with improved cloud
582 screening for Sun photometer aerosol optical depth (AOD) measurements, *Atmos. Meas. Tech.*, 12, 169–209,
583 <https://doi.org/10.5194/amt-12-169-2019>, 2019.

584 Guenther, A. B., Jiang, X., Heald, C. L., Sakulyanontvittaya, T., Duhl, T., Emmons, L. K., and Wang, X.: The
585 Model of Emissions of Gases and Aerosols from Nature version 2.1 (MEGAN2. 1): an extended and updated
586 framework for modeling biogenic emissions, *Geosci. Model Dev.*, 5, 1471–1492, [https://doi.org/10.5194/gmd-5-](https://doi.org/10.5194/gmd-5-1471-2012)
587 1471-2012, 2012.

588 Guo, J., Xia, F., Zhang, Y., Liu, H., Li, J., Lou, M., He, J., Yan, Y., Wang, F., Min, M., and Zhai, P.: Impact of
589 diurnal variability and meteorological factors on the $PM_{2.5}$ - AOD relationship: Implications for $PM_{2.5}$ remote
590 sensing, *Environ. Pollut.*, 221, 94–104, <https://doi.org/10.1016/j.envpol.2016.11.043>, 2017.

591 Guo, H., Campuzano-Jost, P., Nault, B. A., Day, D. A., Schroder, J. C., Dibb, J. E., Dollner, M., Weinzierl, B., and
592 Jimenez, J. L.: The Importance of Size Ranges in Aerosol Instrument Intercomparisons: A Case Study for the ATom
593 Mission, *Atmos. Meas. Tech. Discuss.*, 2020, 1–49, <https://doi.org/10.5194/amt-2020-224>, 2020.

594 Hair, J. W., Hostetler, C. A., Cook, A. L., Harper, D. B., Ferrare, R. A., Mack, T. L., Welch, W., Izquierdo, L. R.,
595 and Hovis, F. E.: Airborne High Spectral Resolution Lidar for profiling aerosol optical properties, *Appl. Opt.*, 47,
596 6734–6752, <https://doi.org/10.1364/AO.47.006734>, 2008.

597 Hammer, M. S., van Donkelaar, A., Li, C., Lyapustin, A., Sayer, A. M., Hsu, N. C., Levy, R. C., Garay, M.,
598 Kalashnikova, O., Kahn, R. A., Brauer, M., Apte, J. S., Henze, D. K., Zhang, L., Zhang, Q., Ford, B., Pierce, J. R.,
599 and Martin, R. V.: Global Estimates and Long-Term Trends of Fine Particulate Matter Concentrations (1998–2018),
600 *Environ. Sci. Technol.*, 54, 7879–7890, <https://dx.doi.org/10.1021/acs.est.0c01764>, 2020.

601 Hu, X., Belle, J. H., Meng, X., Wildani, A., Waller, L. A., Strickland, M. J., and Liu, Y.: Estimating $PM_{2.5}$
602 Concentrations in the Conterminous United States Using the Random Forest Approach, *Environ. Sci. Technol.*, 51,
603 6936–6944, [10.1021/acs.est.7b01210](https://doi.org/10.1021/acs.est.7b01210), 2017.

604 Hudman, R. C., Moore, N. E., Mebust, A. K., Martin, R. V., Russell, A. R., Valin, L. C., and Cohen, R. C.: Steps
605 towards a mechanistic model of global soil nitric oxide emissions: implementation and space based-constraints,
606 *Atmos. Chem. Phys.*, 12, 7779–7795, <https://doi.org/10.5194/acp-12-7779-2012>, 2012.

607 Jaeglé, L., Quinn, P. K., Bates, T. S., Alexander, B., and Lin, J. T.: Global distribution of sea salt aerosols: new
608 constraints from in situ and remote sensing observations, *Atmos. Chem. Phys.*, 11, 3137–3157,
609 <https://doi.org/10.5194/acp-11-3137-2011>, 2011.

610 Jaeglé, L., Shah, V., Thornton, J. A., Lopez-Hilfiker, F. D., Lee, B. H., McDuffie, E. E., Fibiger, D., Brown, S. S.,
611 Veres, P., Sparks, T. L., Ebben, C. J., Wooldridge, P. J., Kenagy, H. S., Cohen, R. C., Weinheimer, A. J., Campos,
612 T. L., Montzka, D. D., Digangi, J. P., Wolfe, G. M., Hanisco, T., Schroder, J. C., Campuzano-Jost, P., Day, D. A.,
613 Jimenez, J. L., Sullivan, A. P., Guo, H., and Weber, R. J.: Nitrogen Oxides Emissions, Chemistry, Deposition, and
614 Export Over the Northeast United States During the WINTER Aircraft Campaign, *J. Geophys. Res. Atmos.*, 123,
615 12,368–312,393, <https://doi.org/10.1029/2018JD029133>, 2018.

616 Jeong, J. I., Park, R. J., and Youn, D.: Effects of Siberian forest fires on air quality in East Asia during May 2003
617 and its climate implication, *Atmos. Environ.*, 42, 8910–8922, <https://doi.org/10.1016/j.atmosenv.2008.08.037>, 2008.

618 Jordan, C. E., Crawford, J. H., Beyersdorf, A. J., Eck, T. F., Halliday, H. S., Nault, B. A., Chang, L.-S., Park, J.,
619 Park, R., and Lee, G.: Investigation of factors controlling PM_{2.5} variability across the South Korean Peninsula during
620 KORUS-AQ, *Elementa-Sci. Anthrop.*, 8, 28, <https://doi.org/10.1525/elementa.424>, 2020.

621 Kim, H., Zhang, Q., and Heo, J.: Influence of intense secondary aerosol formation and long-range transport on
622 aerosol chemistry and properties in the Seoul Metropolitan Area during spring time: results from KORUS-AQ,
623 *Atmos. Chem. Phys.*, 18, 7149-7168, <https://doi.org/10.5194/acp-18-7149-2018>, 2018.

624 Kumar, R., Delle Monache, L., Bresch, J., Saide, P. E., Tang, Y., Liu, Z., da Silva, A. M., Alessandrini, S., Pfister,
625 G., Edwards, D., Lee, P., and Djalalova, I.: Toward Improving Short-Term Predictions of Fine Particulate Matter
626 Over the United States Via Assimilation of Satellite Aerosol Optical Depth Retrievals, *J. Geophys. Res. Atmos.*,
627 124, 2753-2773, <https://doi.org/10.1029/2018JD029009>, 2019.

628 Lamb, K. D., Perring, A. E., Samset, B., Peterson, D., Davis, S., Anderson, B. E., Beyersdorf, A., Blake, D. R.,
629 Campuzano-Jost, P., Corr, C. A., Diskin, G. S., Kondo, Y., Moteki, N., Nault, B. A., Oh, J., Park, M., Pusede, S. E.,
630 Simpson, I. J., Thornhill, K. L., Wisthaler, A., and Schwarz, J. P.: Estimating Source Region Influences on Black
631 Carbon Abundance, Microphysics, and Radiative Effect Observed Over South Korea, *J. Geophys. Res. Atmos.*, 123,
632 13,527-513,548, <https://doi.org/10.1029/2018JD029257>, 2018.

633 Latimer, R. N. C. and Martin, R. V.: Interpretation of measured aerosol mass scattering efficiency over North
634 America using a chemical transport model, *Atmos. Chem. Phys.*, 19, 2635-2653, <https://doi.org/10.5194/acp-19-2635-2019>, 2019.

636 Lee, W., Lim, T., and Kim, D. D.: Thermal and Energy Performance Assessment of the Prefab Electric Ondol
637 System for Floor Heating in a Residential Building, *Energies*, 13, 5723, <https://doi.org/10.3390/en13215723>, 2020.

638 Lennartson, E. M., Wang, J., Gu, J., Castro Garcia, L., Ge, C., Gao, M., Choi, M., Saide, P. E., Carmichael, G. R.,
639 Kim, J., and Janz, S. J.: Diurnal variation of aerosol optical depth and PM_{2.5} in South Korea: a synthesis from
640 AERONET, satellite (GOCI), KORUS-AQ observation, and the WRF-Chem model, *Atmos. Chem. Phys.*, 18,
641 15125-15144, [10.5194/acp-18-15125-2018](https://doi.org/10.5194/acp-18-15125-2018), 2018.

642 Li, K., Liao, H., Zhu, J., and Moch Jonathan, M.: Implications of RCP emissions on future PM_{2.5} air quality and
643 direct radiative forcing over China, *J. Geophys. Res. Atmos.*, 121, 12,985-913,008,
644 <https://doi.org/10.1002/2016JD025623>, 2016.

645 Li, Z., Guo, J., Ding, A., Liao, H., Liu, J., Sun, Y., Wang, T., Xue, H., Zhang, H., and Zhu, B.: Aerosol and
646 boundary-layer interactions and impact on air quality, *Natl. Sci. Rev.*, 4, 810-833, [10.1093/nsr/nwx117](https://doi.org/10.1093/nsr/nwx117), 2017.

647 Lim, H., Choi, M., Kim, J., Kasai, Y., and Chan, P.: AHI/Himawari-8 Yonsei Aerosol Retrieval (YAER):
648 Algorithm, Validation and Merged Products, *Remote Sens.*, 10, 699, <https://doi.org/10.3390/rs10050699>, 2018.

649 Lim, H., Go, S., Kim, J., Choi, M., Lee, S., Song, C. K., and Kasai, Y.: Integration of GOCI and AHI Yonsei aerosol
650 optical depth products during the 2016 KORUS-AQ and 2018 EMeRGe campaigns, *Atmos. Meas. Tech.*, 14, 4575-
651 4592, [10.5194/amt-14-4575-2021](https://doi.org/10.5194/amt-14-4575-2021), 2021.

652 Lin, J. and McElroy, M. B.: Impacts of boundary layer mixing on pollutant vertical profiles in the lower
653 troposphere: Implications to satellite remote sensing, *Atmos. Environ.*, 44, 1726-1739,
654 <https://doi.org/10.1016/j.atmosenv.2010.02.009>, 2010.

655 Liu, H., Jacob, D. J., Bey, I., and Yantosca, R. M.: Constraints from ²¹⁰Pb and ⁷Be on wet deposition and transport in
656 a global three-dimensional chemical tracer model driven by assimilated meteorological fields, *J. Geophys. Res.*
657 *Atmos.*, 106, 12109-12128, <https://doi.org/10.1029/2000JD900839>, 2001.

658 Liu, H., Jacob Daniel, J., Bey, I., Yantosca Robert, M., Duncan Bryan, N., and Sachse Glen, W.: Transport pathways
659 for Asian pollution outflow over the Pacific: Interannual and seasonal variations, *J. Geophys. Res. Atmos.*, 108,
660 8786, <https://doi.org/10.1029/2002JD003102>, 2003.

661 Liu, P., Zhao, C., Liu, P., Deng, Z., Huang, M., Ma, X., and Tie, X.: Aircraft study of aerosol vertical distributions
662 over Beijing and their optical properties, *Tellus B Chem. Phys. Meteorol.*, 61, 756-767, [10.1111/j.1600-0889.2009.00440.x](https://doi.org/10.1111/j.1600-0889.2009.00440.x), 2009.

664 Liu, Y., Park, R. J., Jacob, D. J., Li, Q., Kilaru, V., and Sarnat, J. A.: Mapping annual mean ground-level PM_{2.5}
665 concentrations using Multiangle Imaging Spectroradiometer aerosol optical thickness over the contiguous United
666 States, *J. Geophys. Res. Atmos.*, 109, D22206, <https://doi.org/10.1029/2004JD005025>, 2004.

667 Luo, G., Yu, F., and Moch, J. M.: Further improvement of wet process treatments in GEOS-Chem v12.6.0: impact
668 on global distributions of aerosols and aerosol precursors, *Geosci. Model Dev.*, 13, 2879-2903,
669 <https://doi.org/10.5194/gmd-13-2879-2020>, 2020.

670 Luo, G., Yu, F., and Schwab, J.: Revised treatment of wet scavenging processes dramatically improves GEOS-Chem
671 12.0.0 simulations of nitric acid, nitrate, and ammonium over the United States, *Geosci. Model Dev.*, 12, 3439-3447
672 <https://doi.org/10.5194/gmd-12-3439-2019>, 2019.

673 Martin, R. V., Jacob, D. J., Yantosca, R. M., Chin, M., and Ginoux, P.: Global and regional decreases in
674 tropospheric oxidants from photochemical effects of aerosols, *J. Geophys. Res. Atmos.*, 108, 4097,
675 <https://doi.org/10.1029/2002JD002622>, 2003.

676 McNaughton, C. S., Clarke, A. D., Howell, S. G., Pinkerton, M., Anderson, B., Thornhill, L., Hudgins, C.,
677 Winstead, E., Dibb, J. E., Scheuer, E., and Maring, H.: Results from the DC-8 Inlet Characterization Experiment
678 (DICE): Airborne Versus Surface Sampling of Mineral Dust and Sea Salt Aerosols, *Aerosol Sci. Tech.*, 41, 136-159,
679 <https://doi.org/10.1080/02786820601118406>, 2007.

680 McNaughton, C. S., Clarke, A. D., Kapustin, V., Shinozuka, Y., Howell, S. G., Anderson, B. E., Winstead, E., Dibb,
681 J., Scheuer, E., Cohen, R. C., Wooldridge, P., Perring, A., Huey, L. G., Kim, S., Jimenez, J. L., Dunlea, E. J.,
682 DeCarlo, P. F., Wennberg, P. O., Crouse, J. D., Weinheimer, A. J., and Flocke, F.: Observations of heterogeneous
683 reactions between Asian pollution and mineral dust over the Eastern North Pacific during INTEX-B, *Atmos. Chem.*
684 *Phys.*, 9, 8283-8308, <https://doi.org/10.5194/acp-9-8283-2009>, 2009.

685 Meng, J., Martin, R. V., Ginoux, P., Hammer, M., Sulprizio, M. P., Ridley, D. A., and van Donkelaar, A.: Grid-
686 independent High Resolution Dust Emissions (v1.0) for Chemical Transport Models: Application to GEOS-Chem
687 (version 12.5.0), *Geosci. Model Dev. Discuss.*, 1-23, <https://doi.org/10.5194/gmd-2020-380>, 2020.

688 Miao, R., Chen, Q., Zheng, Y., Cheng, X., Sun, Y., Palmer, P. I., Shrivastava, M., Guo, J., Zhang, Q., Liu, Y., Tan,
689 Z., Ma, X., Chen, S., Zeng, L., Lu, K., and Zhang, Y.: Model bias in simulating major chemical components of
690 PM_{2.5} in China, *Atmos. Chem. Phys.*, 20, 12265-12284, <https://doi.org/10.5194/acp-20-12265-2020>, 2020.

691 Murray, L. T., Jacob, D. J., Logan, J. A., Hudman, R. C., and Koshak, W. J.: Optimized regional and interannual
692 variability of lightning in a global chemical transport model constrained by LIS/OTD satellite data, *J. Geophys. Res.*
693 *Atmos.*, 117, D20307, <https://doi.org/10.1029/2012JD017934>, 2012.

694 Nault, B. A., Campuzano-Jost, P., Day, D. A., Schroder, J. C., Anderson, B., Beyersdorf, A. J., Blake, D. R., Brune,
695 W. H., Choi, Y., Corr, C. A., de Gouw, J. A., Dibb, J., DiGangi, J. P., Diskin, G. S., Fried, A., Huey, L. G., Kim, M.
696 J., Knote, C. J., Lamb, K. D., Lee, T., Park, T., Pusede, S. E., Scheuer, E., Thornhill, K. L., Woo, J. H., and Jimenez,
697 J. L.: Secondary organic aerosol production from local emissions dominates the organic aerosol budget over Seoul,
698 South Korea, during KORUS-AQ, *Atmos. Chem. Phys.*, 18, 17769-17800, [https://doi.org/10.5194/acp-18-17769-](https://doi.org/10.5194/acp-18-17769-2018)
699 2018, 2018.

700 O'Neill, N. T., Eck, T. F., Smirnov, A., Holben, B. N., and Thulasiraman, S.: Spectral discrimination of coarse and
701 fine mode optical depth, *J. Geophys. Res. Atmos.*, 108, <https://doi.org/10.1029/2002JD002975>, 2003.

702 Pai, S. J., Heald, C. L., Pierce, J. R., Farina, S. C., Marais, E. A., Jimenez, J. L., Campuzano-Jost, P., Nault, B. A.,
703 Middlebrook, A. M., Coe, H., Shilling, J. E., Bahreini, R., Dingle, J. H., and Vu, K.: An evaluation of global organic
704 aerosol schemes using airborne observations, *Atmos. Chem. Phys.*, 20, 2637-2665, [https://doi.org/10.5194/acp-20-](https://doi.org/10.5194/acp-20-2637-2020)
705 2637-2020, 2020.

706 Park, R. J., Oak, Y. J., Emmons, L. K., Kim, C.-H., Pfister, G. G., Carmichael, G. R., Saide, P. E., Cho, S.-Y., Kim,
707 S., Woo, J.-H., Crawford, J. H., Gaubert, B., Lee, H.-J., Park, S.-Y., Jo, Y.-J., Gao, M., Tang, B., Stanier, C. O.,
708 Shin, S. S., Park, H. Y., Bae, C., and Kim, E.: Multi-model intercomparisons of air quality simulations for the
709 KORUS-AQ campaign, *Elementa-Sci. Anthropol.*, 9, 00139, <https://doi.org/10.1525/elementa.2021.00139>, 2021.

710 Park Rokjin, J., Jacob Daniel, J., Field Brendan, D., Yantosca Robert, M., and Chin, M.: Natural and transboundary
711 pollution influences on sulfate-nitrate-ammonium aerosols in the United States: Implications for policy, *J. Geophys.*
712 *Res. Atmos.*, 109, D15204, <https://doi.org/10.1029/2003JD004473>, 2004.

713 Pendergrass, D. C., Jacob, D. J., Zhai, S., Kim, J., Koo, J. H., Lee, S., Bae, M., Kim, S.: Continuous mapping of fine
714 particulate matter (PM_{2.5}) air quality in East Asia at daily 6x6 km² resolution by application of a random forest
715 algorithm to 2011-2019 GOCI geostationary satellite data, submitted, 2021.

716 Peterson, D. A., Hyer, E. J., Han, S.-O., Crawford, J. H., Park, R. J., Holz, R., Kuehn, R. E., Eloranta, E., Knote, C.,
717 Jordan, C. E., and Lefer, B. L.: Meteorology influencing springtime air quality, pollution transport, and visibility in
718 Korea, *Elementa-Sci. Anthropol.*, 7, 57, <https://doi.org/10.1525/elementa.395>, 2019.

719 Philip, S., Martin, R. V., Snider, G., Weagle, C. L., van Donkelaar, A., Brauer, M., Henze, D. K., Klimont, Z.,
720 Venkataraman, C., and Guttikunda, S. K.: Anthropogenic fugitive, combustion and industrial dust is a significant,
721 underrepresented fine particulate matter source in global atmospheric models, *Environ. Res. Lett.*, 12, 044018,
722 <https://doi.org/10.1088/1748-9326/aa65a4>, 2017.

723 Podolske, J. R., Sachse, G. W., and Diskin, G. S.: Calibration and data retrieval algorithms for the NASA
724 Langley/Ames Diode Laser Hygrometer for the NASA Transport and Chemical Evolution Over the Pacific
725 (TRACE-P) mission, *J. Geophys. Res. Atmos.*, 108, 8792, <https://doi.org/10.1029/2002JD003156>, 2003.

726 Pye, H. O. T., Liao, H., Wu, S., Mickley, L. J., Jacob, D. J., Henze, D. K., and Seinfeld, J. H.: Effect of changes in
727 climate and emissions on future sulfate-nitrate-ammonium aerosol levels in the United States, *J. Geophys. Res.*
728 *Atmos.*, 114, D01205, <https://doi.org/10.1029/2008JD010701>, 2009.

729 Qu, W., Wang, J., Zhang, X., Sheng, L., and Wang, W.: Opposite seasonality of the aerosol optical depth and the
730 surface particulate matter concentration over the north China Plain, *Atmos. Environ.*, 127, 90-99,
731 <https://doi.org/10.1016/j.atmosenv.2015.11.061>, 2016.

732 Ridley, D. A., Heald, C. L., Kok, J. F., and Zhao, C.: An observationally constrained estimate of global dust aerosol
733 optical depth, *Atmos. Chem. Phys.*, 16, 15097-15117, 10.5194/acp-16-15097-2016, 2016.

734 Saide, P. E., Kim, J., Song, C. H., Choi, M., Cheng, Y., and Carmichael, G. R.: Assimilation of next generation
735 geostationary aerosol optical depth retrievals to improve air quality simulations, *Geophys. Res. Lett.*, 41, 9188-9196,
736 <https://doi.org/10.1002/2014GL062089>, 2014.

737 Saide, P. E., Gao, M., Lu, Z., Goldberg, D. L., Streets, D. G., Woo, J. H., Beyersdorf, A., Corr, C. A., Thornhill, K.
738 L., Anderson, B., Hair, J. W., Nehrir, A. R., Diskin, G. S., Jimenez, J. L., Nault, B. A., Campuzano-Jost, P., Dibb, J.,
739 Heim, E., Lamb, K. D., Schwarz, J. P., Perring, A. E., Kim, J., Choi, M., Holben, B., Pfister, G., Hodzic, A.,
740 Carmichael, G. R., Emmons, L., and Crawford, J. H.: Understanding and improving model representation of aerosol
741 optical properties for a Chinese haze event measured during KORUS-AQ, *Atmos. Chem. Phys.*, 20, 6455-6478,
742 <https://doi.org/10.5194/acp-20-6455-2020>, 2020.

743 Scarino, A. J., Obland, M. D., Fast, J. D., Burton, S. P., Ferrare, R. A., Hostetler, C. A., Berg, L. K., Lefer, B.,
744 Haman, C., Hair, J. W., Rogers, R. R., Butler, C., Cook, A. L., and Harper, D. B.: Comparison of mixed layer
745 heights from airborne high spectral resolution lidar, ground-based measurements, and the WRF-Chem model during
746 CalNex and CARES, *Atmos. Chem. Phys.*, 14, 5547-5560, <https://doi.org/10.5194/acp-14-5547-2014>, 2014.

747 Sekiyama, T. T., Tanaka, T. Y., Shimizu, A., and Miyoshi, T.: Data assimilation of CALIPSO aerosol observations,
748 *Atmos. Chem. Phys.*, 10, 39-49, <https://doi.org/10.5194/acp-10-39-2010>, 2010.

749 Seinfeld, J. H. and Pandis, S. N.: *Atmospheric Chemistry and Physics: From Air Pollution to Climate Change*, Third
750 Edition, Ch. 8, John Wiley & Sons, New Jersey, 2016.

751 Shah, V., Jacob, D. J., Moch, J. M., Wang, X., and Zhai, S.: Global modeling of cloud water acidity, precipitation
752 acidity, and acid inputs to ecosystems, *Atmos. Chem. Phys.*, 20, 12223-12245, <https://doi.org/10.5194/acp-20-12223-2020>, 2020.

754 Su, T., Li, Z., and Kahn, R.: Relationships between the planetary boundary layer height and surface pollutants
755 derived from lidar observations over China: regional pattern and influencing factors, *Atmos. Chem. Phys.*, 18,
756 15921-15935, 10.5194/acp-18-15921-2018, 2018.

757 Sun, X., Yin, Y., Sun, Y., Sun, Y., Liu, W., and Han, Y.: Seasonal and vertical variations in aerosol distribution over
758 Shijiazhuang, China, *Atmos. Environ.*, 81, 245-252, <https://doi.org/10.1016/j.atmosenv.2013.08.009>, 2013.

759 Travis, K. R., Crawford, J. H., Nault, B. A., Kim, H., Jordan, C. E., Chen, G., Zhai, S., Wang, X., Jimenez, J. L.,
760 Dibb, J. E., Brune, W. H., Weinheimer, A., Wennberg, P., Long, R., Szykman, J. J., Woo, J. H., Kim, Y., Li, K.,

761 McDuffie, E., Luo, G., Zhang, Q., Kim, S.: Why do models have difficulty simulating ammonium nitrate and nitric
762 acid in East Asia?, manuscript in preparation.

763 van Donkelaar, A., Martin Randall, V., Brauer, M., and Boys Brian, L.: Use of Satellite Observations for Long-
764 Term Exposure Assessment of Global Concentrations of Fine Particulate Matter, *Environ. Health Perspect.*, 123,
765 135-143, <https://doi.org/10.1289/ehp.1408646>, 2015.

766 van Donkelaar, A., Martin, R. V., Brauer, M., Hsu, N. C., Kahn, R. A., Levy, R. C., Lyapustin, A., Sayer, A. M., and
767 Winker, D. M.: Global Estimates of Fine Particulate Matter using a Combined Geophysical-Statistical Method with
768 Information from Satellites, Models, and Monitors, *Environ. Sci. Technol.*, 50, 3762-3772,
769 <https://doi.org/10.1021/acs.est.5b05833>, 2016.

770 van der Werf, G. R., Randerson, J. T., Giglio, L., van Leeuwen, T. T., Chen, Y., Rogers, B. M., Mu, M., van Marle,
771 M. J. E., Morton, D. C., Collatz, G. J., Yokelson, R. J., and Kasibhatla, P. S.: Global fire emissions estimates during
772 1997–2016, *Earth Syst. Sci. Data*, 9, 697-720, <https://doi.org/10.5194/essd-9-697-2017>, 2017.

773 van Donkelaar, A., Martin, R. V., Li, C., and Burnett, R. T.: Regional Estimates of Chemical Composition of Fine
774 Particulate Matter Using a Combined Geoscience-Statistical Method with Information from Satellites, Models, and
775 Monitors, *Environ. Sci. Technol.*, 53, 2595-2611, [10.1021/acs.est.8b06392](https://doi.org/10.1021/acs.est.8b06392), 2019.

776 van Donkelaar, A., Martin, R. V., and Park, R. J.: Estimating ground-level PM_{2.5} using aerosol optical depth
777 determined from satellite remote sensing, *J. Geophys. Res. Atmos.*, 111, [10.1029/2005JD006996](https://doi.org/10.1029/2005JD006996), 2006.

778 Wang, Q., Jacob, D. J., Fisher, J. A., Mao, J., Leibensperger, E. M., Carouge, C. C., Le Sager, P., Kondo, Y.,
779 Jimenez, J. L., Cubison, M. J., and Doherty, S. J.: Sources of carbonaceous aerosols and deposited black carbon in
780 the Arctic in winter-spring: implications for radiative forcing, *Atmos. Chem. Phys.*, 11, 12453-12473,
781 <https://doi.org/10.5194/acp-11-12453-2011>, 2011.

782 Wang, Q., Jacob, D. J., Spackman, J. R., Perring, A. E., Schwarz, J. P., Moteki, N., Marais, E. A., Ge, C., Wang, J.,
783 and Barrett, S. R. H.: Global budget and radiative forcing of black carbon aerosol: Constraints from pole-to-pole
784 (HIPPO) observations across the Pacific, *J. Geophys. Res. Atmos.*, 119, 195-206,
785 <https://doi.org/10.1002/2013JD020824>, 2014.

786 Wang, X., Heald, C. L., Ridley, D. A., Schwarz, J. P., Spackman, J. R., Perring, A. E., Coe, H., Liu, D., and Clarke,
787 A. D.: Exploiting simultaneous observational constraints on mass and absorption to estimate the global direct
788 radiative forcing of black carbon and brown carbon, *Atmos. Chem. Phys.*, 14, 10989-11010,
789 <https://doi.org/10.5194/acp-14-10989-2014>, 2014.

790 Wang, Y., Zhang, Q., Jiang, J., Zhou, W., Wang, B., He, K., Duan, F., Zhang, Q., Philip, S., and Xie, Y.: Enhanced
791 sulfate formation during China's severe winter haze episode in January 2013 missing from current models, *J.*
792 *Geophys. Res. Atmos.*, 119, 425-410,440, <https://doi.org/10.1002/2013JD021426>, 2014.

793 Wei, J., Li, Z., Pinker, R. T., Wang, J., Sun, L., Xue, W., Li, R., and Cribb, M.: Himawari-8-derived diurnal
794 variations in ground-level PM_{2.5} pollution across China using the fast space-time Light Gradient Boosting Machine
795 (LightGBM), *Atmos. Chem. Phys.*, 21, 7863-7880, [10.5194/acp-21-7863-2021](https://doi.org/10.5194/acp-21-7863-2021), 2021a.

796 Wei, J., Li, Z., Lyapustin, A., Sun, L., Peng, Y., Xue, W., Su, T., and Cribb, M.: Reconstructing 1-km-resolution
797 high-quality PM_{2.5} data records from 2000 to 2018 in China: spatiotemporal variations and policy implications,
798 *Remote Sens. Environ.*, 252, 112136, <https://doi.org/10.1016/j.rse.2020.112136>, 2021b.

799 Woo, J.-H., Kim, Y., Kim, H.-K., Choi, K.-C., Eum, J.-H., Lee, J.-B., Lim, J.-H., Kim, J., and Seong, M.:
800 Development of the CREATE Inventory in Support of Integrated Climate and Air Quality Modeling for Asia,
801 *Sustainability*, 12, 7930, <https://doi.org/10.3390/su12197930>, 2020.

802 Xiao, Q., Chang, H. H., Geng, G., and Liu, Y.: An Ensemble Machine-Learning Model To Predict Historical PM_{2.5}
803 Concentrations in China from Satellite Data, *Environ. Sci. Technol.*, 52, 13260-13269, [10.1021/acs.est.8b02917](https://doi.org/10.1021/acs.est.8b02917),
804 2018.

805 Xu, J., Han, F., Li, M., Zhang, Z., Xiaohui, D., and Wei, P.: On the opposite seasonality of MODIS AOD and
806 surface PM_{2.5} over the Northern China plain, *Atmos. Environ.*, 215, 116909,
807 <https://doi.org/10.1016/j.atmosenv.2019.116909>, 2019.

808 Xu, J. W., Martin, R. V., van Donkelaar, A., Kim, J., Choi, M., Zhang, Q., Geng, G., Liu, Y., Ma, Z., Huang, L.,
809 Wang, Y., Chen, H., Che, H., Lin, P., and Lin, N.: Estimating ground-level PM_{2.5} in eastern China using aerosol
810 optical depth determined from the GOCI satellite instrument, *Atmos. Chem. Phys.*, 15, 13133-13144, 10.5194/acp-
811 15-13133-2015, 2015.

812 Xue, T., Zheng, Y., Tong, D., Zheng, B., Li, X., Zhu, T., and Zhang, Q.: Spatiotemporal continuous estimates of
813 PM_{2.5} concentrations in China, 2000–2016: A machine learning method with inputs from satellites, chemical
814 transport model, and ground observations, *Environ. Int.*, 123, 345-357, <https://doi.org/10.1016/j.envint.2018.11.075>,
815 2019.

816 Zhai, S., Jacob, D. J., Wang, X., Shen, L., Li, K., Zhang, Y., Gui, K., Zhao, T., and Liao, H.: Fine particulate matter
817 (PM_{2.5}) trends in China, 2013-2018: separating contributions from anthropogenic emissions and meteorology,
818 *Atmos. Chem. Phys.*, 19, 11031-11041 <https://doi.org/10.5194/acp-19-11031-2019>, 2019.

819 Zhai, S., Jacob, D. J., Wang, X., Liu, Z., Wen, T., Shah, V., Li, K., Moch, J. M., Bates, K. H., Song, S., Shen, L.,
820 Zhang, Y., Luo, G., Yu, F., Sun, Y., Wang, L., Qi, M., Tao, J., Gui, K., Xu, H., Zhang, Q., Zhao, T., Wang, Y., Lee,
821 H. C., Choi, H., and Liao, H.: Control of particulate nitrate air pollution in China, *Nat. Geosci.*,
822 <https://doi.org/10.1038/s41561-021-00726-z>, 2021.

823 Zhang, L., Kok, J. F., Henze, D. K., Li, Q., and Zhao, C.: Improving simulations of fine dust surface concentrations
824 over the western United States by optimizing the particle size distribution, *Geophys. Res. Lett.*, 40, 3270-3275,
825 <https://doi.org/10.1002/grl.50591>, 2013.

826 Zhang, L., Gong, S., Padro, J., and Barrie, L.: A size-segregated particle dry deposition scheme for an atmospheric
827 aerosol module, *Atmos. Environ.*, 35, 549-560, [https://doi.org/10.1016/S1352-2310\(00\)00326-5](https://doi.org/10.1016/S1352-2310(00)00326-5), 2001.

828 Zhang, Q., Zhao, C., Tie, X., Wei, Q., Huang, M., Li, G., Ying, Z., and Li, C.: Characterizations of aerosols over the
829 Beijing region: A case study of aircraft measurements, *Atmos. Environ.*, 40, 4513-4527,
830 <https://doi.org/10.1016/j.atmosenv.2006.04.032>, 2006.

831 Zhang, Q., Ma, X., Tie, X., Huang, M., and Zhao, C.: Vertical distributions of aerosols under different weather
832 conditions: Analysis of in-situ aircraft measurements in Beijing, China, *Atmos. Environ.*, 43, 5526-5535,
833 <https://doi.org/10.1016/j.atmosenv.2009.05.037>, 2009.

834 Zhang, X., Wang, H., Che, H.-Z., Tan, S.-C., Shi, G.-Y., and Yao, X.-P.: The impact of aerosol on MODIS cloud
835 detection and property retrieval in seriously polluted East China, *Sci. Total Environ.*, 711, 134634,
836 <https://doi.org/10.1016/j.scitotenv.2019.134634>, 2020.

837 Zheng, B., Tong, D., Li, M., Liu, F., Hong, C., Geng, G., Li, H., Li, X., Peng, L., Qi, J., Yan, L., Zhang, Y., Zhao,
838 H., Zheng, Y., He, K., and Zhang, Q.: Trends in China's anthropogenic emissions since 2010 as the consequence of
839 clean air actions, *Atmos. Chem. Phys.*, 18, 14095-14111, <https://doi.org/10.5194/acp-18-14095-2018>, 2018.

840 Ziemba, L. D., Lee Thornhill, K., Ferrare, R., Barrick, J., Beyersdorf, A. J., Chen, G., Crumeyrolle, S. N., Hair, J.,
841 Hostetler, C., Hudgins, C., Obland, M., Rogers, R., Scarino, A. J., Winstead, E. L., and Anderson, B. E.: Airborne
842 observations of aerosol extinction by in situ and remote-sensing techniques: Evaluation of particle hygroscopicity,
843 *Geophys. Res. Lett.*, 40, 417-422, <https://doi.org/10.1029/2012GL054428>, 2013.

844